

Bayesian inference of grid cell firing patterns using Poisson point process models with latent oscillatory Gaussian random fields

Ioannis Papastathopoulos ^{*1}, Graeme Auld ^{†3}, Finn Lindgren ^{‡1}, Klára Zsófia Gerlei ^{§2} and Matthew F. Nolan ^{¶2}

¹School of Mathematics and Maxwell Institute, University of Edinburgh, Edinburgh, EH9 3FD, Scotland

²Centre for Discovery Brain Sciences, University of Edinburgh, Edinburgh, EH8 9XD, Scotland

³Department of Mathematics and Computer Science, Chulalongkorn University, Bangkok, Thailand

Abstract

Questions about information encoded by the brain demand statistical frameworks for inferring relationships between neural firing and features of the world. The landmark discovery of grid cells demonstrates that neurons can represent spatial information through regularly repeating firing fields. However, the influence of covariates may be masked in current statistical models of grid cell activity, which by employing approaches such as discretizing, aggregating and smoothing, are computationally inefficient and do not account for the continuous nature of the physical world. These limitations motivated us to develop likelihood-based procedures for modelling and estimating the firing activity of grid cells conditionally on biologically relevant covariates. Our approach models firing activity using Poisson point processes with latent Gaussian effects, which accommodate persistent inhomogeneous spatio-directional patterns and overdispersion. Inference is performed in a fully Bayesian manner, which allows quantification of uncertainty. Applying these methods to experimental data, we provide evidence for temporal and local head direction effects on grid firing. Our approaches offer a novel and principled framework for analysis of neural representations of space.

Key-words: Cox process, Gaussian field, grid cells, head-directional effect, oscillation, temporal modulation

AMS subject classifications: Primary: 60G60, Secondary: 62M40, 62-07

*i.papastathopoulos@ed.ac.uk

†graemeross.a@chula.ac.th

‡finn.lindgren@ed.ac.uk

§klara.gerlei@ed.ac.uk

¶matt.nolan@ed.ac.uk

1 Introduction

1.1 Motivation: Inferring signals represented by neural activity

What information does the activity of neurons in the brain convey about the world? Questions of this kind are typically addressed by analysing recordings of neural activity, from which spike events are extracted, binned and smoothed (Dayan and Abbott, 2005). However, with such approaches, the continuous nature of the physical world is neglected. This may mask fine scale structure in neural activity and impede assessment of the effect of co-variables. These problems could in principle be addressed by adopting modelling approaches that work on the finest scale possible. Here, we develop such approaches with the goal of analysing the firing patterns of grid cells found in the medial entorhinal cortex.

The medial entorhinal cortex is a critical brain region for spatial cognition and episodic memory (Eichenbaum and Lipton, 2008; Tukker et al., 2022; Gerlei et al., 2021). Neurons in this area are of particular interest because of strong associations between their firing activity and variables related to position and movement through space (Moser et al., 2017). Neurons have been identified that encode locations (Hafting et al., 2005; Solstad et al., 2008), orientation (Sargolini et al., 2006) and speed of movement (Kropff et al., 2015). The main emphasis and focus of this paper is on the statistical modelling of the firing activity of grid cells (Hafting et al., 2005). Grid cells are believed to form a coordinate system that allows spatial navigation and learning of maps of the world. The metric of this representation is provided by spatial firing fields that tile environments in a periodic hexagonal pattern. The left panel of Figure 1 shows a typical data set consisting of a trajectory of an animal (grey), that is, a record of the path followed by a moving animal over a period of time, and an associated point pattern (black dots) of the locations at which action potentials of a grid cell are observed. The action potentials are termed *firing events*. More information about how the data were collected can be found in Section 4.1.

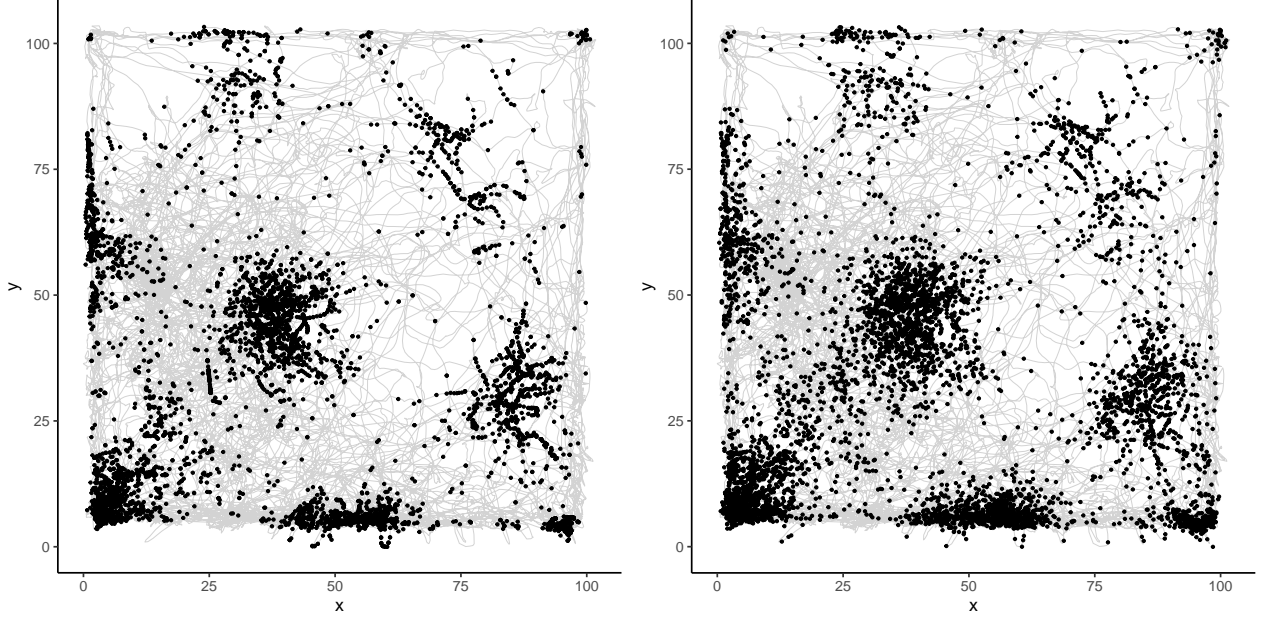


Figure 1: Left: True point pattern data (shown in black) on a trajectory Γ_Ω (shown in grey). Right: Simulated data on Γ_Ω from an inhomogeneous Poisson point process with estimated intensity function $\hat{\lambda}_{\Gamma_\Omega}^0$ given by expression (1).

1.2 Current approaches for inferring grid cell activity

Current approaches for inferring the intensity of grid firing events rely mainly on kernel smoothing methods. Such methods are based on the *firing rate map* which is an estimator of the rate of occurrence of firing events per unit time at any spatial location (Sargolini et al., 2006). The estimator is defined by

$$\hat{\lambda}_{\mathcal{T}}^0(s; h) = \int_0^T K_h(\|\Gamma_\Omega(t) - s\|) N_{\mathcal{T}}(dt) / \int_0^T K_h(\|\Gamma_\Omega(t) - s\|) dt, \quad s \in \mathbb{R}^2, T > 0, h > 0, \quad (1)$$

where $\Gamma_\Omega : [0, T] \rightarrow \mathbb{R}^2$ denotes a continuously differentiable curve with $\Gamma_\Omega(t) = (s_x(t), s_y(t))$ representing the location of the animal in \mathbb{R}^2 at time $t \in \mathcal{T} := [0, T]$ and $N_{\mathcal{T}}$ denotes the counting process of firing events over time. The kernel function K_h is defined by $K_h(s) = K(s/h)/h$, $s \in \mathbb{R}^2$, where K denotes the probability density of the bivariate Gaussian distribution with mean vector $(0, 0)$ and variance-covariance matrix equal to the identity matrix $I_2 \in \mathbb{R}^{2 \times 2}$. The parameter h is a bandwidth parameter and $\|\cdot\|$ denotes

the Euclidean norm. In what follows, time is measured in seconds, distances in centimeters and angles in radians.

To understand estimator (1), it is helpful to decompose it into the product of two estimators, one associated with the expected number of firing events per unit distance travelled at location s , and the other associated with the expected speed of the animal at location s . In particular, if we denote

$$W_h(t, s) = K_h(\|\Gamma_\Omega(t) - s\|) / \int_0^T K_h(\|\Gamma_\Omega(t) - s\|) dt \quad \text{and} \quad \dot{\Gamma}_\Omega(t) = \left(\frac{ds_x(t)}{dt}, \frac{ds_y(t)}{dt} \right),$$

then we have that $\widehat{\lambda}_\mathcal{T}^0(s; h) = \widehat{\lambda}_{\Gamma_\Omega}^0(s; h) \widehat{v}(s; h)$, where

$$\begin{aligned} \widehat{\lambda}_{\Gamma_\Omega}^0(s; h) &= \int_0^T K_h(\|\Gamma_\Omega(t) - s\|) N_\mathcal{T}(dt) / \int_{\Gamma_\Omega} K_h(\|z - s\|) dz, \\ \widehat{v}(s; h) &= \int_{\Gamma_\Omega} K_h(\|z - s\|) dz / \int_0^T K_h(\|\Gamma_\Omega(t) - s\|) dt = \int_0^T W_h(t, s) \|\dot{\Gamma}_\Omega(t)\| dt, \end{aligned}$$

with $\int_{\Gamma_\Omega} g(z) dz$ denoting the line integral of an arbitrary integrable scalar field $g : \mathbb{R}^2 \rightarrow \mathbb{R}$ along the curve Γ_Ω . Thus, $\widehat{\lambda}_\mathcal{T}^0$ decomposes into the product of a kernel-smoothing based estimator $\widehat{\lambda}_{\Gamma_\Omega}^0$ for the intensity of a non-homogeneous Poisson point process on the trajectory Γ_Ω (Diggle, 1985) and a kernel-smoothing based estimator $\widehat{v}(s; h)$ of the expected speed of the animal at a given location s . This estimator is intrinsically non-parametric, but it assumes that for any interval of time $I \subseteq \mathcal{T}$ with $|I| > 0$, the variation in the counts of firing events $N_\mathcal{T}(I)$ that are observed during I is solely explained by how much area the animal explores and what regions it visits in this period of time.

Whilst seemingly simple, estimator (1) can be unwieldy. First, kernel smoothing methods may mask fine scale structure in the data and may produce overly smooth estimates. Although there are data-driven methods for choosing the bandwidth parameter, fixing it to $h = 3\text{cm}$ (*cf.* Sargolini et al., 2006, supplementary material) appears to be common

practice. Contrasting a realization of an inhomogeneous Poisson point process on Γ_Ω , with intensity function equal to $\widehat{\lambda}_{\Gamma_\Omega}^0(\cdot, 3)$ (Figure 1, right panel), with the ground-truth data (left panel), we see an effect of oversmoothing, e.g., in the bottom left region of the square arena. The ground-truth data exhibit an additional amount of clustering which is also not captured by the inhomogeneous Poisson point process. This questions the validity of the estimator and of the generic use of a fixed bandwidth parameter.

To the best of our knowledge, no systematic study on the smoothness properties of the firing activity of grid-cells exists. Although estimator (1) is continuously specified, it is typically computed by discretizing the spatial domain and then by using aggregated statistics such as counts of firing events. The counts are then used to estimate the firing activity. Although this simplifies statistical modelling, it comes at a cost as it reduces estimation efficiency and may lead to ecological bias, whereby inferences obtained at the coarser scale are incorrectly carried over to the finer scale.

Second, the assumption that the variation in the number of counts $N_{\mathcal{T}}(I)$ is explained only by the animal's locations in the period of time I may not be sufficient. For example, the firing activity may also be explained by covariates other than the location of the animal such as the orientation of its head, which we will refer to as the head-direction. By discretizing the domain of the covariates and by computing counts within each part of the domain, Gerlei et al. (2020) gave evidence for an interaction effect between the location and the head-direction, with variations in the firing activity explained by combinations of locations and head-directions. Again, the concern of potential ecological bias due to discretization and aggregation effects also extends to the approach adopted by Gerlei et al. (2020).

In this paper we are led to develop new statistical procedures for modelling the firing activity of grid cells that are flexible, extendible, and coherent at the finest possible scale. This requires a step-change in approach relative to current methodology and practice. In particular, we adopt a principled statistical approach based on log-Gaussian Cox processes.

Our approach bypasses issues related to ecological bias as it avoids discretization and aggregation. Additionally, it allows inclusion of covariates in a straightforward manner. We build a range of statistical models which include biologically relevant covariates. We show better predictive performance from a model that includes an effect of interaction between the location and the head-direction of the animal, thereby confirming the results of Gerlei et al. (2020). Our proposed statistical models are hierarchical and are built on the assumption that the intensity function is random, and its prior distribution is determined by that of a stationary Gaussian process. Owing to the strong oscillatory nature of the firing activity, we use Gaussian processes with underdamped Matérn covariance functions (Lindgren et al., 2011). The upshot of this choice is that our prior distributions mimic closely the effect of the covariates in the firing activity, and the fitting of the models can be performed efficiently due to the compactly supported basis function representation of our proposed Gaussian random fields. As a by-product, we give closed-form expressions for the marginal variance of Gaussian processes on \mathbb{R} , \mathbb{R}^2 , and $\mathbb{S}_1 = [0, 2\pi)$, with underdamped, critically damped, and overdamped Matérn covariances. We build our models in a Bayesian framework, which gives us a tool for fitting complex models, and the advantage of doing this efficiently with integrated nested Laplace approximation (INLA, Rue et al., 2009). We use the R package `inlabru` (Bachl et al., 2019), which is based on INLA and is specialized in dealing with structured data and has extensive support for point process models.

1.3 Paper structure

In Section 2 we describe the statistical framework that use throughout the paper. Preliminary notation associated with the experimental framework is presented Section 2.1. Section 2.2 introduces the class of log-Gaussian Cox processes and Section 2.3 describes a general framework for including covariates in the intensity function of a Poisson point process. Section 2.4 discusses the finite-dimensional Gaussian Markov random field (GMRF)

approximations of the latent Gaussian random fields that we use to model the effect of covariates on the firing rate of grid cells. In Section 2.5 we describe the properties of the continuous limit Gaussian random fields that the GMRFs presented in Section 2.4 converge to, and derive closed-form expressions for the variances, which are necessary for practical model fitting and the interpretation of the models. Section 3 details practical information about how we perform inference in practice. In particular, in Section 3.1 we present approximate closed-form expressions for the likelihood function and describe the numerical integration scheme that we use to evaluate the intractable integral associated with the void probability of each Poisson point process model. In Section 3.2, we complete the specification of the Bayesian models through choices of appropriate prior distributions for the hyperparameters. Section 4 contains our implementation, analysis and interpretation of the proposed models through a case study example from the grid cell spike train shown in Figure 1. The data set is described in Section 4.1. In Section 4.2, we assess the predictive performance of all models via cross-validation and in 4.3 we fit and interpret all models to the data. We conclude with a discussion that highlights the strengths of the methodology in Section 5. Technical material and additional supporting evidence is presented in 6 (Supplementary Material).

2 Statistical modelling

2.1 Notation and framework

The standard experimental framework relates to an animal; typically a rodent moving in the interior of a bounded planar domain $\Omega \subset \mathbb{R}^2$; and is modelled by a filtered probability space $(E, \mathcal{H}, \mathbf{P}, \mathcal{F})$ where $\mathcal{F} = (\mathcal{F}_t)_{t \in \mathbb{R}_+}$ denotes an increasing family of sub- σ -algebras of \mathcal{H} . The animal moves freely for a period of time $\mathcal{T} = [0, T]$, where $T : E \rightarrow \mathbb{R}_+$ denotes a stopping time, i.e., $\{T \leq t\} \in \mathcal{F}_t$ for all $t > 0$. The stopping time T marks

the end of the experiment and in practice, it is usually decided prior to the start of the experiment. Hence, we assume T is non-informative. For any $t \in \mathcal{T}$, let the two-dimensional vector $\Gamma_\Omega(t) = (s_x(t), s_y(t))^\top \in \mathbb{R}^2$ denote the spatial co-ordinates of the animal in Ω at time t , $\Gamma_\Omega(A) = \{\Gamma_\Omega(t) : t \in A\}$, $A \subseteq \mathcal{T}$, and $\Gamma_\Omega := \Gamma_\Omega(\mathcal{T})$ for the continuously differentiable curve in Ω representing the entire trajectory of spatial locations of the animal throughout the duration of the experiment. Let $\{s_0 := \Gamma_\Omega(\tau_0), \dots, s_N := \Gamma_\Omega(\tau_N)\}$ be a sample of locations taken from Γ_Ω at approximately regular times $\tau_0, \tau_1, \dots, \tau_N \in \mathcal{T}$, i.e., $\tau_{i+1} - \tau_i \approx \Delta\tau > 0$. Let also $\theta(t) \in \mathbb{S}_1 := [0, 2\pi)$ denote the head-direction of the animal at time t and write $\{\theta_0 := \theta(\tau_0), \dots, \theta_N := \theta(\tau_N)\}$ for the sample of head-directions. Prior to time $\tau_0 = 0$, electrodes that measure the firing activity of a nerve cell are implanted in the brain of the animal. Let $f : E \rightarrow \{0, 1\}^\mathcal{T}$ be a random variable from the sample space E to the set of all functions on \mathcal{T} with image $\{0, 1\}$. For a fixed realization of the experiment the function f encodes the activity of the neuron according to the convention: $f(t) = 1$, if the neuron is active at time t and $f(t) = 0$, otherwise. In what follows, it is assumed that available are the labeled data $\{(s_1, \theta_1, f(\tau_1)), \dots, (s_N, \theta_N, f(\tau_N))\}$. We write t_1, \dots, t_n for the set of times the neuron is active, that is, $\{t_i : i = 1, \dots, n\} = \{\tau_j : f(\tau_j) = 1\}$.

2.2 Cox processes

Let $N_\mathcal{T} : E \times \mathcal{H} \rightarrow (\mathbb{R}_+, \mathcal{B}(\mathbb{R}_+))$ be a random counting measure on $(\mathbb{R}_+, \mathcal{B}(\mathbb{R}_+))$, that is, $e \mapsto N_\mathcal{T}(e, A)$ is a random variable for each $A \in \mathcal{B}(\mathbb{R}_+)$ and $A \mapsto N_\mathcal{T}(e, A)$ is, for almost every $e \in E$, a purely atomic measure and its every atom has weight one. We shall denote by $N_\mathcal{T}(A)$ the former random variable and we will associate with it the number of firing events in a Borel subset A of time. Let also $\Lambda_\mathcal{T} : E \times \mathcal{H} \rightarrow (\mathbb{R}_+, \mathcal{B}(\mathbb{R}_+))$ be a random measure on $(\mathbb{R}_+, \mathcal{B}(\mathbb{R}_+))$ satisfying, $\Lambda_\mathcal{T}(A) = \int_A \lambda_\mathcal{T}(t) dt$ for any $A \in \mathcal{B}(\mathbb{R}_+)$, where $\lambda_\mathcal{T} = (\lambda_\mathcal{T}(t))_{t \in \mathbb{R}_+}$ is a positive continuous stochastic process. In what follows, we say that the counting process $N_\mathcal{T}$ follows a Cox process with random intensity $\lambda_\mathcal{T}$ if the

conditional expectation of $\exp(-N_{\mathcal{T}}f)$ given the sigma-algebra \mathcal{F} generated by $\Lambda_{\mathcal{T}}$ is

$$\mathbb{E} \{ \exp(-N_{\mathcal{T}}f) \mid \mathcal{F} \} = \exp \left(- \int_{\mathbb{R}_+} [1 - \exp\{-f(t)\}] \lambda_{\mathcal{T}}(t) dt \right), \quad f \in \mathcal{B}(\mathbb{R}_+), \quad f \geq 0,$$

that is, conditionally on the intensity function $\lambda_{\mathcal{T}}$, the process $N_{\mathcal{T}}$ is an inhomogeneous Poisson point process with intensity $\lambda_{\mathcal{T}}$ on \mathcal{T} , meaning that for any countable collection of disjoint subsets $A_1, \dots, A_k \subseteq \mathcal{B}(\mathbb{R}_+)$, we have

$$N_{\mathcal{T}}(A_i) \mid \lambda_{\mathcal{T}} \sim \text{Poisson} \left(\int_{A_i} \lambda_{\mathcal{T}}(t) dt \right) \text{ and } N_{\mathcal{T}}(A_1), \dots, N_{\mathcal{T}}(A_k) \text{ are independent given } \lambda_{\mathcal{T}}.$$

Cox processes have been applied in various fields such as ecology, epidemiology, neuroscience, and image analysis. This is because Cox processes can model point patterns that exhibit both clustering and inhomogeneity, which is a trait observed in many natural phenomena. Another reason for the widespread use of Cox processes is their flexibility and capacity for statistical modelling. The requirements that are needed on the properties of $\lambda_{\mathcal{T}}$ so that $N_{\mathcal{T}}$ exists are minimal and this accommodates a broad class of models for the random intensity function $\lambda_{\mathcal{T}}$. Amongst the most popular ones, the log-Gaussian Cox process (LGCP) models the logarithm of the random intensity of the point process $N_{\mathcal{T}}$ as a Gaussian process, which allows for flexible modelling of the variability of the point pattern, and can model the effect of covariates in a non-linear manner. LGCPs are also useful for Bayesian inference, as the Gaussian process prior facilitates efficient numerical algorithms.

Given the σ -field \mathcal{F} generated by $\Lambda_{\mathcal{T}}$ and a point pattern $\{t_1, \dots, t_n\}$ in a bounded set $\mathcal{T} \subset \mathbb{R}_+$, the likelihood of an inhomogeneous Poisson process is

$$L(\lambda_{\mathcal{T}}) = \exp \left[\int_{\mathcal{T}} \{1 - \lambda_{\mathcal{T}}(t)\} dt \right] \prod_{i=1}^n \lambda_{\mathcal{T}}(t_i). \quad (2)$$

Because likelihoods are needed up to a proportionality factor, expression (2) is often pre-

sented without the term “1” that appears in the exponent in the first factor. Such a simplification in the likelihood function (2) is valid provided the domain of the point process remains unchanged. However, when one is interested in modelling and inferring the distribution of $N_{\mathcal{T}}$ subject to changes in its domain, then (2) cannot be simplified further.

2.3 Statistical models for spike trains from grid cells

To facilitate generality, we define the configuration space of the system to be the set of allowable positions relative to a reference state. For example, consider an animal whose body is moving in a two dimensional Euclidean space and whose orientation in space is changing according to a direction in the unit circle. Then we may take the configuration space to be the Riemannian manifold $\mathbb{R}^2 \times \mathbb{S}_1$. More generally, we can label the configuration of the animal by a system of generalized coordinates $x = (x_1, \dots, x_m)$, where $x_j \in \mathcal{X}_j \subseteq \mathbb{R}^{d_j}$, $j = 1, \dots, m$, $d_j, m \in \mathbb{N}$, so that for the aforementioned example, we have $x_1 = (s_x, s_y)$ and $x_2 = \theta$ with (s_x, s_y) denoting the row vector of Cartesian coordinates in $\mathcal{X}_1 = \mathbb{R}^2$ and θ denoting an angle in $\mathcal{X}_2 = \mathbb{S}_1 = [0, 2\pi)$. In the course of an experiment, the animal undergoes dynamical evolution so it continuously changes its position. This evolution can be specified by giving the generalized coordinate location of the animal as a function of time, that is, $(x_1, \dots, x_m) = (x_1(t), \dots, x_m(t))$ for $t \in \mathcal{T}$. This defines a curve of covariates $\Gamma = \{\Gamma(t) : t \in \mathcal{T}\}$ where $\Gamma(t) = (x_1(t), \dots, x_m(t))$ which we assume to be continuously differentiable. It is worth to remark here that prior to the start of the experiment, Γ is unknown. Hence, Γ may be taken to be a random element, that is, a map that is measurable relative to \mathcal{H} and $\mathcal{B}(\mathcal{X})$, where $\mathcal{X} := \prod_{j=1}^m \mathcal{X}_j$. In a Bayesian setting, this assumption is equivalent to treating Γ as a statistical parameter in a hierarchical statistical model. Such an approach would allow inference to be made about the dynamics of the trajectory of the animal and potentially, about its effects on the intensity of the point pattern, via the assignment of a prior distribution on Γ and via posterior updating of prior beliefs. However,

owing to the fact that there is no evidence for an effect from the dynamics of Γ on the firing properties of grid-cells, which is the main application and emphasis of this paper, we shall henceforth treat the trajectory as known and fixed a priori, and we will construct statistical models conditionally on the curve Γ .

To model the effect of the covariates on the number of spikes per unit time at time t , we need to link the random mean measure $\Lambda_{\mathcal{T}}$ to a random measure on \mathcal{X} . This is accomplished by specifying $\Lambda_{\mathcal{T}}$ in terms of a mapping l that is measurable relative to the join sigma-algebra $\mathcal{B}(\mathcal{X}) \vee \mathcal{B}(\mathcal{T})$ and the sigma-algebra $\mathcal{B}(\mathbb{R}_+)$, that is, $\Lambda_{\mathcal{T}}(dt) = l(d\Gamma(t), dt)$. To define the distance near each point of the smooth manifold \mathcal{X} , we endow \mathcal{X} with a Riemannian metric that specifies infinitesimal distances on \mathcal{X} . A Riemannian metric assigns to each x a positive-definite inner product $g_x : T_x \mathcal{X} \times T_x \mathcal{X} \rightarrow \mathbb{R}$ where $T_x \mathcal{X}$ is the tangent space at x . Given a system of generalized coordinates $x : U \rightarrow \mathbb{R}^{\sum_j d_j}$ on an open set U of \mathcal{X} , the vectors $(\partial/\partial x_1|_x, \dots, \partial/\partial x_m|_x)$ form a basis of the vector space $T_x \mathcal{X}$ for any $x \in U$. Relative to this basis, we define the metric components of a metric tensor $G = (g_{ij|x})_{1 \leq i, j \leq m}$ at each x by $g_{ij|x} = g_x(\partial/\partial x_i|_x, \partial/\partial x_j|_x)$. With this notation, our general modelling framework presupposes that the expected number of spikes per unit time at time t equals to the expected number of spikes per unit generalized travel distance at generalized coordinate $x(t)$, multiplied by the generalized speed of the particle at time t . This is compactly written as

$$\Lambda_{\mathcal{T}}(dt) = \lambda_{\mathcal{T}}(t) dt = \|\dot{x}(t)\| \lambda_{\mathcal{X}}(x(t)), \quad (3)$$

where $\|\dot{x}(t)\|^2 = \{(dx(t)/dt)^\top G (dx(t)/dt)\}$ and $\|\dot{x}(t)\|$ is the local derivative of the geodesic metric induced by the Riemannian metric G along the curve Γ (Adler and Taylor, 2007). Here $\log \lambda_{\mathcal{X}}$ is a real-valued stochastic process on \mathcal{X} .

A natural choice for the metric tensor G in our setting is $G = \text{diag}(1, 1, \delta)$ where δ is

measured in meters per radians, that is, the metric tensor only involves an axis aligned scaling in the direction of θ , which gives $\|\dot{x}(t)\|^2 = \dot{s}_x(t)^2 + \dot{s}_y(t)^2 + \delta \dot{\theta}(t)^2$. The parameter δ is an unknown parameter and in our implementations, we selected a prior distribution degenerate at 0, which implies that firing events cannot occur due changes in the head-direction of the animal whilst the animal stays still; this choice was motivated by subject expert knowledge and for the simplicity it affords. Thus, in our implementation we use $\|\dot{x}(t)\| = \|\dot{\Gamma}_\Omega(t)\|$ which is the speed of the animal. However, it is worth to remark that, should there be need for the use of a different prior for δ , then this parameter could be inferred even if instances in the data where the animal stays still have been filtered out.

Based on these choices, in this paper we consider the models

$$\mathcal{M}_\Omega : \Lambda_{\mathcal{T}}(dt) = \Lambda_\Omega(\Gamma_\Omega(dt)) := \|\dot{\Gamma}_\Omega(t)\| \lambda_\Omega(\Gamma_\Omega(t)),$$

$$\mathcal{M}_{\Omega, \mathcal{T}} : \Lambda_{\mathcal{T}}(dt) = \Lambda_{\Omega, \mathcal{T}}(\Gamma_\Omega(dt), dt) := \|\dot{\Gamma}_\Omega(t)\| \lambda_\Omega(\Gamma_\Omega(t)) h_{\mathcal{T}}(t),$$

$$\mathcal{M}_{\Omega \times \Theta} : \Lambda_{\mathcal{T}}(dt) = \Lambda_{\Omega \times \Theta}(\Gamma_\Omega(dt), \theta(dt)) := \|\dot{\Gamma}_\Omega(t)\| \lambda_{\Omega \times \Theta}(\Gamma_\Omega(t), \theta(t)),$$

$$\mathcal{M}_{\Omega \times \Theta, \mathcal{T}} : \Lambda_{\mathcal{T}}(dt) = \Lambda_{\Omega \times \Theta, \mathcal{T}}(\Gamma_\Omega(dt), \theta(dt), dt) := \|\dot{\Gamma}_\Omega(t)\| \lambda_{\Omega \times \Theta}(\Gamma_\Omega(t), \theta(t)) h_{\mathcal{T}}(t),$$

where λ_Ω , $\lambda_{\Omega \times \Theta}$ and $h_{\mathcal{T}}$ denote positive continuous stochastic process on Ω , $\Omega \times \Theta$ and \mathcal{T} , respectively, and are described in detail in Sections 2.4 and 2.5.

Model \mathcal{M}_Ω assumes that the variation in the number of spikes is solely explained by how much area the animal explores and what regions it visits in a period of time. In particular, in \mathcal{M}_Ω , the expected number of spikes per unit time at time t is the product of the expected number of spikes per travel distance at location $\Gamma_\Omega(t)$, which is measured by $\lambda_\Omega(\Gamma_\Omega(t))$, with the speed of the animal at time t , which is measured by $\|\dot{\Gamma}_\Omega(t)\|$. Hence, \mathcal{M}_Ω is similar in spirit with the model formulation and estimator (1) of [Sargolini et al. \(2006\)](#) that we presented in Section 1.2, and hence, it will serve as our baseline model. Model $\mathcal{M}_{\Omega \times \Theta}$ assumes that the variation in the number of spikes is explained by how much area

the animal explores and what regions in $\mathbb{R} \times \mathbb{S}_1$ it visits in a period of time. Specifically, in $\mathcal{M}_{\Omega, \mathcal{T}}$, the expected number of spikes per unit time at time t is the product of the expected number of spikes per travel distance at the generalized coordinate $(\Gamma_{\Omega}(t)^{\top}, \theta(t))$, which is measured by $\lambda_{\Omega \times \Theta}(\Gamma_{\Omega}(t), \theta(t))$, with the speed of the animal at time t .

Models $\mathcal{M}_{\Omega, \mathcal{T}}$ and $\mathcal{M}_{\Omega \times \Theta, \mathcal{T}}$ include an additional factor $h_{\mathcal{T}}$ which modulates the firing rate as a function of experimental clock time, see for example [Kass and Ventura \(2001\)](#) for a similar construction. Here, the stochastic process $h_{\mathcal{T}}$ is dimensionless and hence, the interpretation of λ_{Ω} and $\lambda_{\Omega \times \Theta}$ is identical to that in models \mathcal{M}_{Ω} and $\mathcal{M}_{\Omega \times \Theta}$, respectively. The rationale for including a modulating factor in models $\mathcal{M}_{\Omega, \mathcal{T}}$ and $\mathcal{M}_{\Omega \times \Theta, \mathcal{T}}$ stems from the likely scenario of additional, unobserved covariates, explaining variation in the number and properties of firing events which is not explained by λ_{Ω} or $\lambda_{\Omega \times \Theta}$ alone.

2.4 Continuously specified finite-dimensional Gaussian random fields

Inference can be facilitated through specification of the law of the stochastic process $\lambda_{\mathcal{X}}$. The most common and practically useful choice is that of $\lambda_{\mathcal{X}}$ being a log-Gaussian process, i.e., a random field on \mathcal{X} for which the finite-dimensional distributions of $(\log \lambda_{\mathcal{X}}(x_1), \dots, \log \lambda_{\mathcal{X}}(x_m))$ are multivariate Gaussian for each $1 \leq m \leq \infty$ and each $(x_1, \dots, x_m) \in \mathcal{X}$.

The firing rate per unit displacement per unit generalized distance at generalized coordinate $x \in \mathcal{X}$, and the modulating factor are modelled as $\log \lambda_{\mathcal{X}}(x) = \beta + \xi_{\mathcal{X}}(x)$ and $\log h_{\mathcal{T}}(t) = \xi_{\mathcal{T}}(t)$, where β denotes a background constant firing rate and $\xi_{\mathcal{X}}$ and $\xi_{\mathcal{T}}$ are stationary zero-mean Gaussian processes on \mathcal{X} and \mathcal{T} , respectively. Specifying a joint covariance structure over $\mathcal{X} = \mathcal{X}_1 \times \dots \times \mathcal{X}_m$ is highly demanding and it is natural to simplify this task by treating the joint covariance as separable in the input of the random field $\xi_{\mathcal{X}}$, i.e., to assume the covariance function has a Kronecker product form (see [Rougier, 2008](#)) which asserts that $\text{cov}(\xi(x), \xi(x')) = \prod_{i=1}^m \zeta_i(x_i, x'_i)$, $x, x' \in \mathcal{X}$, where $\zeta_i : \mathcal{X}_i \rightarrow \mathbb{R}$ is a valid covariance function, i.e., a non-negative definite function on \mathcal{X}_i .

For the differentiable manifolds $\mathcal{X}_1 := \Omega \subset \mathbb{R}^2$ and $\mathcal{X}_2 := \Theta := [0, 2\pi)$, we specify the latent random fields using the finite dimensional models $\xi_\Omega(s) = \boldsymbol{\psi}^\Omega(s)^\top \mathbf{w}^\Omega$, $\xi_\Theta(\theta) = \boldsymbol{\psi}^\Theta(\theta)^\top \mathbf{w}^\Theta$, $\xi_{\Omega \times \Theta}(s, \theta) = \boldsymbol{\psi}^\Theta(\theta)^\top \mathbf{w}^{\Omega \times \Theta} \boldsymbol{\psi}^\Omega(s)$ and $\xi_{\mathcal{T}}(t) = \boldsymbol{\psi}^\mathcal{T}(t)^\top \mathbf{w}^\mathcal{T}$, where $\mathbf{w}_{p_\Omega \times 1}^\Omega \sim \mathbf{N}(\mathbf{0}, \mathbf{Q}_\Omega(\boldsymbol{\chi}_\Omega)^{-1})$, $\mathbf{w}_{p_\Theta \times 1}^\Theta \sim \mathbf{N}(\mathbf{0}, \mathbf{Q}_\Theta(\boldsymbol{\chi}_\Theta)^{-1})$, $\text{vec}((\mathbf{w}_{p_\Theta \times p_\Omega}^{\Omega \times \Theta})^\top)_{(p_\Omega p_\Theta) \times 1} \sim \mathbf{N}(\mathbf{0}, \mathbf{Q}_\Omega(\boldsymbol{\chi}_\Omega)^{-1} \otimes \mathbf{Q}_\Theta(\boldsymbol{\chi}_\Theta)^{-1})$, and $\mathbf{w}_{p_\mathcal{T} \times 1}^\mathcal{T} \sim \mathbf{N}(\mathbf{0}, \mathbf{Q}_\mathcal{T}(\boldsymbol{\chi}_\mathcal{T})^{-1})$, are independent vectors of stochastic weights; $\boldsymbol{\psi}^\Omega = (\psi_i^\Omega : i = 1, \dots, p_\Omega)$, $\boldsymbol{\psi}^\Theta = (\psi_j^\Theta : j = 1, \dots, p_\Theta)$, and $\boldsymbol{\psi}^\mathcal{T} = (\psi_k^\mathcal{T} : k = 1, \dots, p_\mathcal{T})$, are deterministic piecewise linear basis functions on \mathbb{R}^2, Θ and \mathbb{R} , defined for each node on a spatial, circular, and temporal mesh, respectively; vec and \otimes denote vectorization of a matrix by stacking its column vectors on top of one another and Kronecker product, respectively; and $\mathbf{Q}_\Omega(\boldsymbol{\chi}_\Omega)$, $\mathbf{Q}_\Theta(\boldsymbol{\chi}_\Theta)$ and $\mathbf{Q}_\mathcal{T}(\boldsymbol{\chi}_\mathcal{T})$ are positive-definite precision matrices defined by $\mathbf{Q}_\cdot(\boldsymbol{\chi}_\cdot) = \tau^2(\kappa^4 C + 2\varphi \cdot \kappa^2 G + G C^{-1} G)$, where $\boldsymbol{\chi}_\cdot = (\kappa, \tau, \varphi)$, $\kappa, \tau > 0$, $\varphi \in (-1, \infty)$, $C = (C_{rc})_{r,c=1}^{p_\cdot}$ with $C_{rc} = \langle \psi_r, \psi_c \rangle$, and $G = (G_{rc})_{r,c=1}^{p_\cdot}$ with $G_{rc} = \langle \nabla \psi_r, \nabla \psi_c \rangle$. Here, \cdot is used as a placeholder for Ω, Θ and \mathcal{T} and $\langle \psi_r, \psi_c \rangle := \int \psi_r(e) \psi_c(e) \lambda(e)$, where λ denotes the Lebesgue measure on the respective domain.

The vectors of stochastic weights belong to the class of Gaussian Markov random fields (GMRF) (Rue and Held, 2005) and their Markovian properties are determined by the graph structure of the mesh. The weights control the stochastic properties of $\xi_\Omega, \xi_\Theta, \xi_{\Omega \times \Theta}$ and $\xi_{\mathcal{T}}$, and are chosen so that the distribution of each linear combination converges to the distribution of the solution of an SPDE, see Simpson et al. (2016) for more details.

2.5 Limiting infinite-dimensional Gaussian random fields

When the parameters φ_Ω and φ_Θ are equal to unity, then all random fields presented in Section 2.4 converge strongly (Lindgren et al., 2011; Simpson et al., 2016) to Gaussian random fields with Matérn covariance functions, a class of random fields that is widely adopted in spatial statistics (Stein, 1999). In particular, the models that we presented in the previous section are Hilbert space projections of solutions of the Whittle–Matérn stochastic

(partial) differential equation (Lindgren et al., 2011, 2022). The continuously specified infinite-dimensional limits of the Gaussian random fields ξ_Ω , ξ_Θ and $\xi_\mathcal{T}$ are Gaussian random fields with power spectral mass/density functions

$$f_\Omega(\boldsymbol{\omega}) = \frac{\sigma_\Omega^2}{(2\pi)^2} \left(\frac{1}{\kappa_\Omega^4 + 2\varphi_\Omega \kappa_\Omega^2 \|\boldsymbol{\omega}\|^2 + \|\boldsymbol{\omega}\|^4} \right)^{\alpha_\Omega/2}, \quad \boldsymbol{\omega} \in \mathbb{R}^2 \quad (4)$$

$$f_\Theta(\omega) = \frac{\sigma_\Theta^2}{2\pi} \left(\frac{1}{\kappa_\Theta^4 + 2\varphi_\Theta \kappa_\Theta^2 \omega^2 + \omega^4} \right)^{\alpha_\Theta/2}, \quad \omega \in \mathbb{Z} \quad (5)$$

$$f_\mathcal{T}(\omega) = \frac{\sigma_\mathcal{T}^2}{2\pi} \left(\frac{1}{\kappa_\mathcal{T}^4 + 2\varphi_\mathcal{T} \kappa_\mathcal{T}^2 \omega^2 + \omega^4} \right)^{\alpha_\mathcal{T}/2}, \quad \omega \in \mathbb{R}. \quad (6)$$

respectively, where the shape parameters satisfy $\alpha_\Omega = \alpha_\Theta = \alpha_\mathcal{T} = 2$. We work with the special case where all shape parameters are equal to 2, for the simplicity and clarity this choice affords. The covariance functions may be given in analytic form for some cases only, e.g., on \mathbb{R} and \mathbb{R}^2 , inversion of the spectrum gives (Lindgren et al., 2011)

$$\begin{aligned} \zeta_\Omega(s) &= \frac{\sigma_\Omega^2}{4\pi \sin(\pi\gamma_\Omega) \kappa_\Omega^2 i} \left[K_0 \left\{ \kappa_\Omega \|s\| \exp\left(-\frac{i\pi\gamma_\Omega}{2}\right) \right\} - K_0 \left\{ \kappa_\Omega \|s\| \exp\left(\frac{i\pi\gamma_\Omega}{2}\right) \right\} \right], \\ \zeta_\mathcal{T}(t) &= \frac{\sigma_\mathcal{T}^2}{2 \sin(\pi\gamma_\mathcal{T}) \kappa_\mathcal{T}^3} \exp\left\{-\kappa_\mathcal{T} \cos\left(\frac{\pi\gamma_\mathcal{T}}{2}|t|\right)\right\} \sin\left\{\frac{\pi\gamma_\mathcal{T}}{2} + \kappa_\mathcal{T} \sin\left(\frac{\pi\gamma_\mathcal{T}}{2}|t|\right)\right\}, \end{aligned}$$

where $\varphi_\Omega, \varphi_\mathcal{T} \in (-1, 1]$ and $\gamma_\cdot = \arccos(\varphi_\cdot)/\pi$. On \mathbb{S}_1 the covariance is obtained in analytic form only for the case $\varphi_\Theta = 1$ and is given in Proposition 1 below.

Proposition 1. *A stationary Gaussian process $\xi_\Theta(\theta)$, $\theta \in \mathbb{S}_1$, with power spectrum (5) with $\varphi_\Theta = 1$, has covariance function*

$$\begin{aligned} \zeta_\Theta(\theta) &= \frac{\sigma_\Theta^2}{4 \sinh^2(\pi\kappa_\Theta) \kappa_\Theta^2} \left\{ \frac{|\theta|}{2} \cosh\{(2\pi - |\theta|)\kappa_\Theta\} + \right. \\ &\quad \left. + \left(\pi - \frac{|\theta|}{2} \right) \cosh(|\theta|\kappa_\Theta) + \kappa_\Theta^{-1} [\cosh\{(\pi - |\theta|)\kappa_\Theta\} \sinh(\pi\kappa_\Theta)] \right\}. \end{aligned}$$

A proof is given in Section 6.2 of the supplement. Although the covariance is available

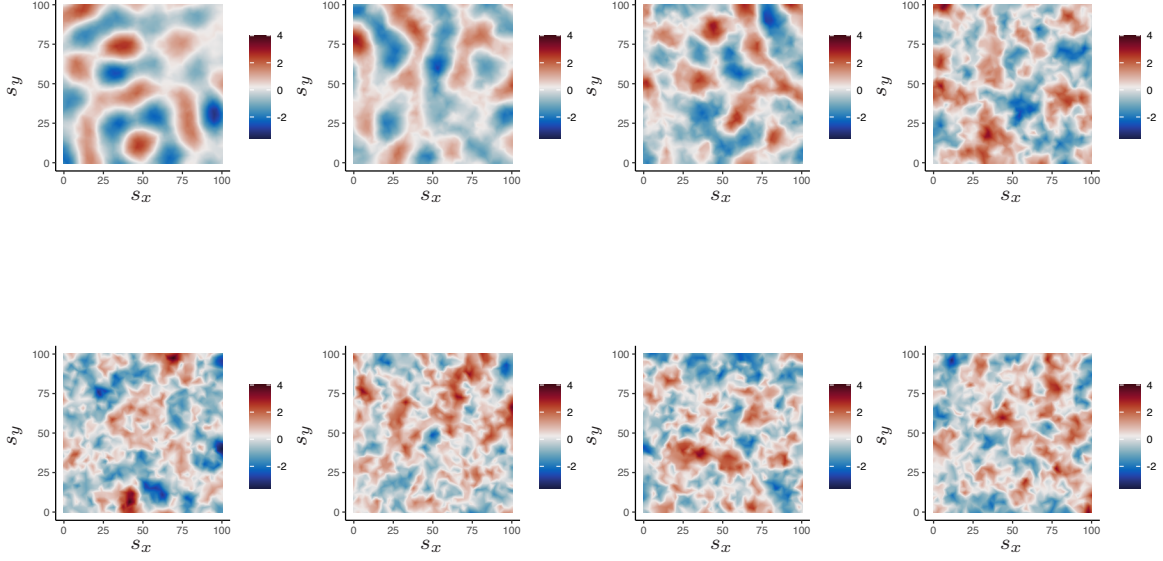


Figure 2: Realizations of a zero-mean Gaussian random field $\xi_\Omega(s)$ with spectral density (4), where $\alpha_\Omega = 2$, $\kappa_\Omega = 0.2$ and $s_\Omega^2 = 1$. *Top, left to right:* shown for $\varphi_\Omega = -9.99/10, -9.9/10, -9/10, -2/10$. *Bottom, right to left:* shown for $\varphi_\Omega = 2/10, 9/10, 9.9/10, 9.99/10$.

in closed-form only under special cases, this is not a substantial inconvenience, as what is needed for practical model fitting are the discretised precision matrices from Section 2.4, and for convenience, e.g. for normalisation and parameter interpretation, the marginal variance. The marginal variances for the processes on \mathbb{R}^2 , \mathbb{S}_1 and \mathbb{R} are given in Propositions 2, 3 and 4.

Proposition 2. *A stationary Gaussian process $\xi_\Omega(s)$, $s \in \mathbb{R}^2$, with power spectrum (4) has marginal variance $s_\Omega^2 := \text{var}\{\xi_\Omega(s)\}$ given by*

$$s_\Omega^2 = \begin{cases} \frac{\sigma_\Omega^2}{4\pi\kappa_\Omega^2\sqrt{1-\varphi_\Omega^2}} \arccos \varphi_\Omega, & \text{underdamped, } \varphi_\Omega \in (-1, 1), \\ \frac{\sigma_\Omega^2}{4\pi\kappa_\Omega^2}, & \text{critically damped, } \varphi_\Omega = 1, \\ \frac{\sigma_\Omega^2}{4\pi\kappa_\Omega^2\sqrt{\varphi_\Omega^2-1}} \left\{ \frac{\pi}{2} - \text{atan} \left(\frac{\varphi_\Omega}{\sqrt{\varphi_\Omega^2-1}} \right) \right\}, & \text{overdamped, } \varphi_\Omega \in (1, \infty). \end{cases}$$

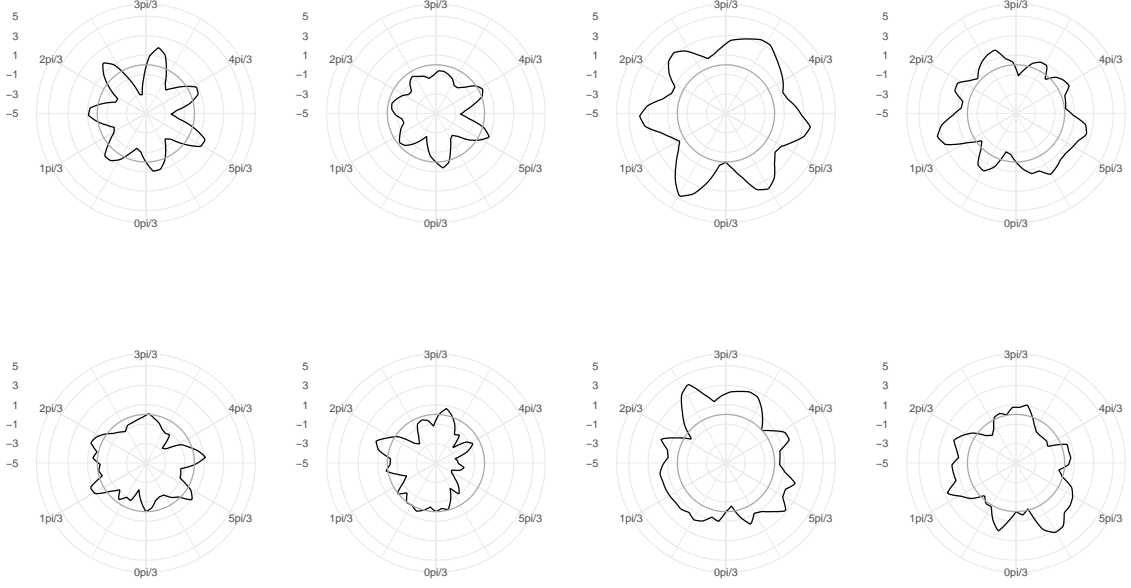


Figure 3: Realizations of $\xi_{\Theta}(\theta) - \xi_{\Theta}(0)$ where ξ_{Θ} is a zero-mean Gaussian random field with spectral mass function (5), where $\alpha_{\mathcal{T}} = 2$, $\kappa_{\Theta} = 2\pi$ and $s_{\Theta}^2 = 1$. Realizations are plotted in polar coordinates, with scale units marked by circles (center refers to scale value -5 and outer circle refers to scale value 5). The circle shown in dark grey refers to the scale value 0 . *Top, left to right*: shown for $\varphi_{\Theta} = -9.99/10, -9.9/10, -9/10, -2/10$. *Bottom, right to left*: shown for $\varphi_{\Theta} = 2/10, 9/10, 9.9/10, 9.99/10$.

Proposition 3. *A stationary Gaussian process $\xi_{\Theta}(\theta)$, $\theta \in \mathbb{S}_1$, with power spectrum (5) has marginal variance $s_{\Theta}^2 := \text{var}\{\xi_{\Theta}(\theta)\}$ given by*

$$s_{\Theta}^2 = \begin{cases} \frac{\sigma_{\Theta}^2}{4\kappa_{\Theta}^3 \sqrt{1 - \phi_{\Theta}^2}} \frac{2\{y \sin(2\pi\kappa_{\Theta}x) + x \sinh(2\pi\kappa_{\Theta}y)\}}{\{\cos(2\pi\kappa_{\Theta}x) - \cosh(2\pi\kappa_{\Theta}y)\}} & \text{underdamped, } \varphi_{\Theta} \in (-1, 1) \\ \frac{\sigma_{\Theta}^2}{4\kappa_{\Theta}^3} & \text{critically damped, } \varphi_{\Theta} = 1 \\ \frac{\sigma_{\Theta}^2}{4\kappa_{\Theta}^3 \sqrt{\varphi_{\Theta}^2 - 1}} \left(\frac{\cot(iz)}{iz} - \frac{\cot(i\bar{z})}{i\bar{z}} \right), & \text{overdamped, } \varphi_{\Theta} \in (1, \infty) \end{cases}$$

where $x = \cos(\gamma/2)$, $y = \sin(\gamma/2)$ and $\gamma \in [-\pi, 0)$ satisfies $\exp(\iota\gamma) = -\phi_{\Theta} - \sqrt{1 - \phi_{\Theta}^2}$.

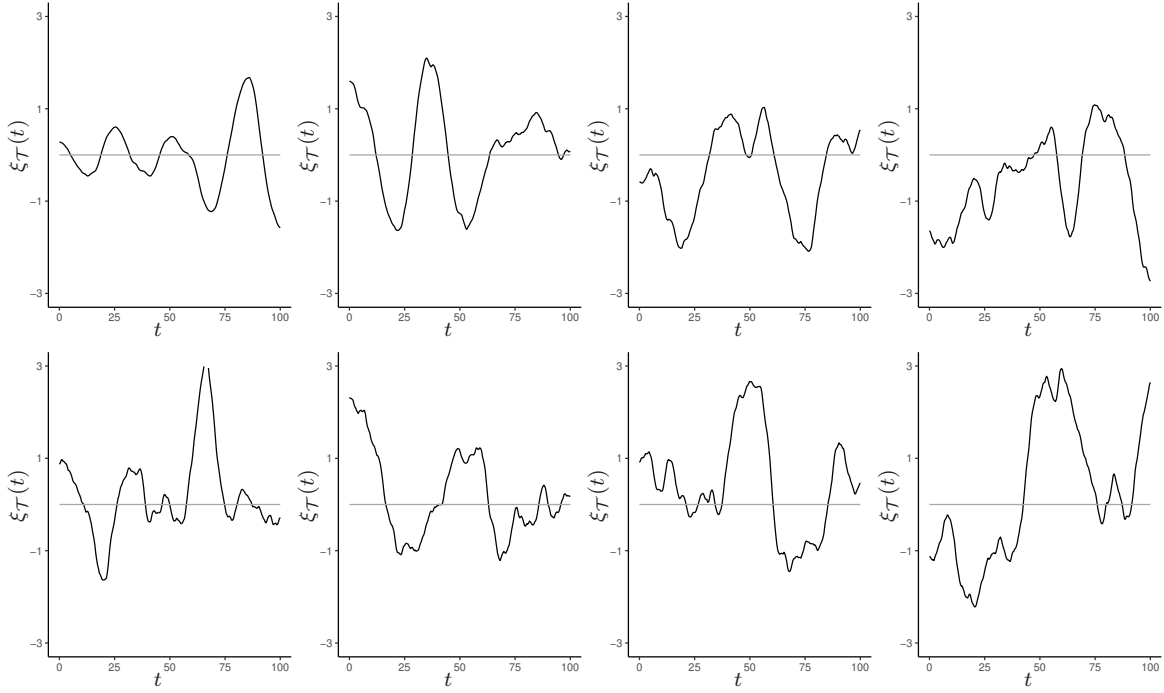


Figure 4: Realizations of $\xi_{\mathcal{T}}(t)$ where $\xi_{\mathcal{T}}$ is a zero-mean Gaussian random field with spectral density (6), where $\alpha_{\mathcal{T}} = 2$, $\kappa_{\mathcal{T}} = 2/10$ and $s_{\mathcal{T}}^2 = 1$. *Top, left to right*: shown for $\varphi_{\mathcal{T}} = -9/10, -7/10, -4/10, -1/10$. *Bottom, right to left*: shown for $\varphi_{\mathcal{T}} = 1/10, 4/10, 7/10, 9/10$.

Proposition 4. A stationary Gaussian process $\xi_{\mathcal{T}}(t)$, $t \in \mathbb{R}_+$, with power spectrum (6) has marginal variance $s_{\mathcal{T}}^2 := \text{var}\{\xi_{\mathcal{T}}(t)\}$ given by

$$s_{\mathcal{T}}^2 = \frac{\sigma_{\mathcal{T}}^2}{4\kappa_{\mathcal{T}}^3} \left(\frac{2}{1 + \varphi_{\mathcal{T}}} \right)^{1/2}, \quad \varphi_{\mathcal{T}} > -1,$$

and is underdamped for $\varphi_{\mathcal{T}} \in (-1, 1)$, critically damped for $\varphi_{\mathcal{T}} = 1$, and overdamped for $\varphi_{\mathcal{T}} > 1$.

Proofs of Propositions 2 3 and 4 are given in Section 6.3 of the supplement.

3 Practical computation and parameter construction

3.1 Numerical evaluation of log-likelihood functions

The logarithm of the likelihood function (2) consists of two terms: a stochastic integral and the evaluation of the random field at the data points. Hence, the log-likelihood is

analytically intractable as it requires the integral of the intensity function which cannot be calculated explicitly. The integral can, however, be approximated numerically using the approach of [Simpson et al. \(2016\)](#) who introduced a computationally efficient method for performing inference on log-Gaussian Cox processes based on continuously specified finite-dimensional Gaussian random fields. The remainder of this section describes the integration schemes that we use for the integrals in the log-likelihood functions of models \mathcal{M}_Ω , $\mathcal{M}_{\Omega, \mathcal{T}}$, $\mathcal{M}_{\Omega \times \Theta}$, and $\mathcal{M}_{\Omega \times \Theta, \mathcal{T}}$, that is, the integration scheme that is used for the integrals

$$\begin{aligned}
I_\Omega &= -e^\beta \sum_{i=1}^N \int_{t_{i-1}}^{t_i} \exp [\boldsymbol{\psi}^\Omega \{s(t)\}^\top \boldsymbol{w}^\Omega] \Gamma_\Omega(dt), \\
I_{\Omega, \mathcal{T}} &= -e^\beta \sum_{i=1}^N \int_{t_{i-1}}^{t_i} \exp [\boldsymbol{\psi}^\Omega \{s(t)\}^\top \boldsymbol{w}^\Omega + \boldsymbol{\psi}^\mathcal{T}(t)^\top \boldsymbol{w}^\mathcal{T}] \Gamma_\Omega(dt), \\
I_{\Omega \times \Theta} &= -e^\beta \sum_{i=1}^N \int_0^T \exp [\boldsymbol{\psi}^{\Omega \times \Theta} \{s(t), \theta(t)\}^\top \boldsymbol{w}^{\Omega \times \Theta}] \Gamma_\Omega(dt), \quad \text{and} \\
I_{\Omega \times \Theta, \mathcal{T}} &= -e^\beta \sum_{i=1}^N \int_0^T \exp \left[\sum \boldsymbol{\psi}^{\Omega \times \Theta} \{s(t), \theta(t)\}^\top \boldsymbol{w}^{\Omega \times \Theta} + \boldsymbol{\psi}^\mathcal{T}(t)^\top \boldsymbol{w}^\mathcal{T} \right] \Gamma_\Omega(dt).
\end{aligned}$$

To ensure a numerically stable and computationally efficient integration scheme, we use the construction of [Yuan et al. \(2017\)](#) and split every straight line segment $L_i = \{(s(t), \theta(t)) : t \in [t_{i-1}, t_i]\} \subset \Omega \times \Theta$ into straight line segments $L_{ij} \subset \Omega \times \Theta$, $j = 1, \dots, J_i$, $J_i \in \mathbb{N}$, each of which resides in exactly one prism in $\Omega \times \Theta$ that is shaped by a distinct triangle in the spatial mesh and a distinct arc in the circular mesh. To simplify the notation, we set $(\tilde{L}_i : i = 0, \dots, \tilde{N}) = (L_{ij} : i = 0, \dots, N, j = 1, \dots, J_i)$, where the elements in the latter vector appear in lexicographic order, so that \tilde{L}_{i-1} and \tilde{L}_i correspond to adjacent line segments, and $\tilde{N} = \sum_{i=0}^N J_i$. This segmentation induces, for $i = 0, \dots, \tilde{N}$, a set of times \tilde{t}_i , locations $s(\tilde{t}_i)$ and head-direction angles $\theta(\tilde{t}_i)$, which are computed via linear interpolation.

Using the trapezoidal rule with based on the partition $\{\tilde{t}_i\}$ of the interval \mathcal{T} , yields

$$\begin{aligned} e^{-\beta} I_{\Omega} &\doteq - \sum_{i=1}^{\tilde{N}} \frac{|\tilde{L}_i|}{2} [\exp(\boldsymbol{\psi}^{\Omega}\{s(\tilde{t}_{i-1})\}^{\top} \mathbf{w}^{\Omega}) + \exp(\boldsymbol{\psi}^{\Omega}\{s(\tilde{t}_i)\}^{\top} \mathbf{w}^{\Omega})] \\ &\doteq - \sum_{i=1}^{\tilde{N}} \frac{|\tilde{L}_i|}{2} [\boldsymbol{\psi}^{\Omega}\{s(\tilde{t}_{i-1})\}^{\top} \exp(\mathbf{w}^{\Omega}) + \boldsymbol{\psi}^{\Omega}\{s(\tilde{t}_i)\}^{\top} \exp(\mathbf{w}^{\Omega})] = -(\mathbf{b}^{\Omega})^{\top} \exp(\mathbf{w}^{\Omega}) \end{aligned} \quad (7)$$

where $\mathbf{b}_{\Omega} = (b_k^{\Omega}) \in \mathbb{R}^{p_{\Omega}}$ with $b_k^{\Omega} = \sum_{i=1}^{\tilde{N}} (|\tilde{L}_i|/2) \sum_{j=i-1}^i \psi_k^{\Omega}\{s(\tilde{t}_j)\}$. We remark that the last approximation in expression (7) follows after replacing $h_j(t) = \exp[\boldsymbol{\psi}^{\Omega}\{s(\tilde{t}_j)\}^{\top} \mathbf{w}^{\Omega}]$ by its linear interpolant which agrees with $h_j(t)$, $j \in \{i-1, i\}$, at the corners of the triangle within which the projection of \tilde{L}_i on Ω resides. The integration scheme that is used for $I_{\Omega \times \Theta}$ is identical to that used for I_{Ω} though it is useful to note that the aforementioned approximation based on linear interpolation is done in the same way except now the linear interpolant matches the function at the corners of the prism in $\Omega \times \Theta$ within which \tilde{L}_i resides. This gives the approximation $e^{-\beta} I_{\Omega \times \Theta} \doteq -(\mathbf{b}^{\Omega \times \Theta})^{\top} \exp(\mathbf{w}^{\Omega \times \Theta})$ where $\mathbf{b}^{\Omega \times \Theta} \in \mathbb{R}^{p_{\Omega} p_{\Theta}}$ with $b_k^{\Omega \times \Theta} = \sum_{i=1}^{\tilde{N}} (|\tilde{L}_i|/2) \sum_{j=i-1}^i \psi_k^{\Omega \times \Theta}\{s(\tilde{t}_j), \theta(\tilde{t}_j)\}$.

The creation of the sequence of successive time points $\{\tilde{t}_i\}_{i=0}^{\tilde{N}}$ allows a simple construction of a mesh on \mathcal{T} that can be used to construct $h_{\mathcal{T}} = \log \xi_{\mathcal{T}}$ in models $\mathcal{M}_{\Omega, \mathcal{T}}$ and $\mathcal{M}_{\Omega \times \Theta, \mathcal{T}}$. Although $\{\tilde{t}_j\}_{i=0}^{\tilde{N}}$ may be used directly as a temporal mesh for the construction of $\xi_{\mathcal{T}}$, there is a computational caveat with such an approach since the requirement of having a fine resolution both for the spatial and directional meshes, which is needed to ensure the GMRF approximation is accurate, may lead to an extremely large number of knots on \mathcal{T} . Therefore, the set $\{\tilde{t}_i\}$ is thinned by choosing a subsequence $\{\tilde{t}_{i_j}\}_{j=0}^{p_{\mathcal{T}}-1}$. This allows to reduce the number of mesh knots on \mathcal{T} and ensures that each line segment $\{(t, s(t)) : t \in [\tilde{t}_{i-1}, \tilde{t}_i]\} \subset \Omega \times \mathcal{T}$ resides in one, and only one, prism shaped by a distinct triangle in the spatial mesh, a distinct arc in the circular mesh and a distinct time interval in the temporal mesh. Using this temporal mesh, then the composite trapezoidal rule with

partition $\{\tilde{t}_i\}_{i=0}^{\tilde{N}}$ yields the approximation

$$e^{-\beta} I_{\Omega, \mathcal{T}} \doteq -\exp(\mathbf{w}^{\mathcal{T}})^{\top} \mathbf{B}^{\Omega, \mathcal{T}} \exp(\mathbf{w}^{\Omega}), \quad \text{where } \mathbf{B}^{\Omega, \mathcal{T}} = (b_{rc}^{\Omega, \mathcal{T}}) \in \mathbb{R}^{p_{\mathcal{T}} \times p_{\Omega}}, \text{ with}$$

$$b_{rc}^{\Omega, \mathcal{T}} = \sum_{i=1}^{\tilde{N}} (|\tilde{L}_i|/2) \sum_{j=i-1}^i [\psi_c^{\Omega} \{s(\tilde{t}_j)\} \psi_r^{\mathcal{T}}(\tilde{t}_j)], \quad r = 1, \dots, p_{\mathcal{T}}, \quad c = 1, \dots, p_{\Omega}$$

These approximations yield the following approximate likelihoods

$$\begin{aligned} \ell(\boldsymbol{\theta}^{\Omega} \mid \mathcal{M}_{\Omega}) &\doteq -e^{\beta} (\mathbf{b}^{\Omega})^{\top} \exp(\mathbf{w}^{\Omega}) + n\beta + \mathbf{1}_n^{\top} \mathbf{A}_{\text{obs}}^{\Omega} \mathbf{w}^{\Omega} \\ \ell(\boldsymbol{\theta}^{\Omega, \mathcal{T}} \mid \mathcal{M}_{\Omega, \mathcal{T}}) &\doteq -e^{\beta} \exp(\mathbf{w}^{\mathcal{T}})^{\top} \mathbf{B}^{\Omega, \mathcal{T}} \exp(\mathbf{w}^{\Omega}) + n\beta + \mathbf{1}_n^{\top} \mathbf{A}_{\text{obs}}^{\Omega, \mathcal{T}} \mathbf{w}^{\Omega, \mathcal{T}} \\ \ell(\boldsymbol{\theta}^{\Omega \times \Theta} \mid \mathcal{M}_{\Omega \times \Theta}) &\doteq -e^{\beta} (\mathbf{b}^{\Omega \times \Theta})^{\top} \exp(\mathbf{w}^{\Omega \times \Theta}) + n\beta + \mathbf{1}_n^{\top} \mathbf{A}_{\text{obs}}^{\Omega \times \Theta} \mathbf{w}^{\Omega \times \Theta} \\ \ell(\boldsymbol{\theta}^{\Omega \times \Theta, \mathcal{T}} \mid \mathcal{M}_{\Omega \times \Theta, \mathcal{T}}) &\doteq -e^{\beta} \exp(\mathbf{w}^{\mathcal{T}})^{\top} \mathbf{B}^{\Omega \times \Theta, \mathcal{T}} \exp(\mathbf{w}^{\Omega \times \Theta}) + n\beta + \mathbf{1}_n^{\top} (\mathbf{A}_{\text{obs}}^{\mathcal{T}} \mathbf{w}^{\mathcal{T}} + \mathbf{A}_{\text{obs}}^{\Omega \times \Theta} \mathbf{w}^{\Omega \times \Theta}) \end{aligned}$$

for \mathcal{M}_{Ω} , $\mathcal{M}_{\Omega, \mathcal{T}}$, $\mathcal{M}_{\Omega \times \Theta}$ and $\mathcal{M}_{\Omega \times \Theta, \mathcal{T}}$, respectively. We remark that the resulting approximate posterior distributions are close to the true posterior since all expressions for the likelihoods can be written in the form given by equation (3) in [Simpson et al. \(2016\)](#).

3.2 Prior distributions of hyperparameters

The full Bayesian hierarchical model is completed upon specification of the joint prior distribution of all hyperparameters in the model. We consider the transformations $\rho_{\Omega} = \sqrt{8}/\kappa_{\Omega}$, $\rho_{\Theta} = \sqrt{8(3/2)}/\kappa_{\Theta}$ and $\rho_{\mathcal{T}} = \sqrt{8(3/2)}/\kappa_{\mathcal{T}}$. The choice of $\sqrt{8}$ and $\sqrt{8(3/2)}$ in the definition of ρ_{Ω} and $\rho_{\mathcal{T}}$ follows [Lindgren et al. \(2011\)](#) and makes ρ_{Ω} and $\rho_{\mathcal{T}}$ the distance and time at which the correlation of the processes ξ_{Ω} and $\xi_{\mathcal{T}}$ is approximately 0.1, respectively. For the cyclic processes ξ_{Θ} , the interpretation of κ_{Θ} depends on whether this parameter is large or small. For large κ_{Θ} , the cyclic aspect can be ignored, and the interpretation in the cyclic Whittle-Matérn model is that the correlation range is also $\sqrt{8\nu_{\Theta}}/\kappa_{\Theta}$, where $\nu_{\Theta} = \alpha_{\Theta} - d/2 = 3/2$ denotes the smoothness parameter of the prior process. If $\sqrt{8\nu_{\Theta}}/\kappa_{\Theta}$

is small relative to 2π , then this value is proportional to the correlation range, that is, it is again the distance at which the correlation is approximately 0.1, and this also holds for a wide range of ν_Θ -values and not only for the special case $\nu_\Theta = 3/2$ that we consider here. However, when κ_Θ is small enough for that nominal correlation range to become close to or larger than 2π , the cyclic behaviour of the process kicks in and the correlation no longer gets close to zero, instead the covariance function ζ_Θ grows close to an increasing constant, plus a cosine function and additional terms associated with higher frequencies in the spectrum. This latter case did not appear to be particularly troublesome in our experiments and hence, we proceed by using the aforementioned reparameterizations.

In what follows, a random variable ϕ is said to follow a location-scale-Beta(a, b, ℓ, u) distribution, if $\phi =^d \ell + (u - \ell)X$, where $X \sim \text{Beta}(a, b)$, with $a, b > 0$. We assume

$$\begin{aligned} \varphi_\Omega &\sim \text{location-scale-Beta}(a_\Omega, b_\Omega, \ell, u), & \varphi_\Theta &\sim \delta_{\{1\}}, & \varphi_\mathcal{T} &\sim \delta_{\{1\}} \\ \rho_\Omega &\sim \text{log-Normal}(\mu_\Omega, \varsigma_\Omega^2), & \rho_\Theta &\sim \text{Exp}(\eta_\Theta), & \rho_\mathcal{T} &\sim \text{Exp}(\eta_\mathcal{T}), \\ s_\Omega &\sim \text{Exp}(\nu_\Omega), & s_\Theta &\sim \text{Exp}(\nu_\Theta), & s_\mathcal{T} &\sim \text{Exp}(\nu_\mathcal{T}), \end{aligned}$$

where $\delta_{\{1\}}$ denotes the Dirac delta distribution at $\{1\}$, $\ell = -1$, $u = 1$, $a_\Omega, b_\Omega, \varsigma_\Omega, \eta_\Theta, \eta_\mathcal{T}, \nu_\Omega, \nu_\Theta, \nu_\mathcal{T} \in \mathbb{R}_+$ and $\mu_\Omega \in \mathbb{R}$. The rationale for choosing an exponential distribution for the standard deviation parameters s_Ω, s_Θ and $s_\mathcal{T}$, and the correlation range parameters ρ_Θ and $\rho_\mathcal{T}$, is the memoryless property, indicating that we are, a priori, claiming relative ignorance about the marginal standard deviation and the scale of the process. On the other hand, a log-Normal prior for ρ_Ω was chosen to include prior knowledge on the range of the spatial process, by centering the distribution to sensible range values.

Regarding the damping coefficients $\varphi_\Omega, \varphi_\Theta$ and $\varphi_\mathcal{T}$, we initially used a location-scale-Beta with $\ell = -1$ and $u = 1$ so that the prior distribution is supported on the interval $(-1, 1)$. That is, we initially constrained all damping coefficients so that the prior Gaussian

random fields associated with the spatial, directional and temporal effects were underdamped. Our results confirmed strong evidence for underdamped behaviour in the spatial effect, but no evidence for underdamped behaviour in the directional and temporal effects. Hence, in what follows we use a degenerate prior distribution at $\{1\}$.

4 Case study

4.1 The grid-cell data

We used data from a study that reports the activity of grid cells in the medial entorhinal cortex of mice exploring a square arena with a polarizing cue on one of the walls (Gerlei et al. (2020)). The recordings were made with tetrodes inserted into the brain and attached to chronically implanted microdrives. Recording sessions were for a maximum of 90 minutes. A camera was attached above the arena to track the position and head-direction of mice. The voltage data were acquired using the OpenEphys platform (Siegle et al., 2017), spike events detected and then clustered using MountainSort (Chung et al., 2017). The detected clusters were evaluated based on quality metrics for isolation, noise-overlap and peak signal to noise ratio (Chung et al., 2017). Clusters with firing rate $> 0.5\text{Hz}$, isolation > 0.9 and noise overlap < 0.05 were retained.

Grid cells were identified using established metrics (Sargolini et al., 2006). Pure grid cells were identified as neurons with a grid score ≥ 0.4 and head-direction cells as cells with a head-direction score ≥ 0.5 . Conjunctive grid cells were defined as cells that passed both the grid cell and head-direction cell criteria. Here, we report data from 1 pure grid cell from 1 mouse.

4.2 Cross-validation

We compare the predictive performance of each model via 50-50% cross-validation. The full trajectory of the mouse is split up into connected segments of fixed lengths, half of which are selected as training data. Specifically, we partition the time domain $\mathcal{T} = [0, T]$ into M consecutive non-overlapping intervals A_1, \dots, A_M of size $\tau = T/M$ seconds. The two training sets are defined via the observed point pattern in A_1, A_3, \dots and in A_2, A_4, \dots , respectively, whilst the test sets are formed by the complementary intervals, that is, by A_2, A_4, \dots and by A_1, A_3, \dots , respectively.

We use proper scoring rules ([Gneiting and Raftery, 2007](#)) to evaluate the performance of models based on their ability to predict the number of firing events on segments from the training set. The scoring rules that we consider are negatively oriented so that smaller scores correspond to better predictions. A negatively oriented scoring rule S is called proper if $\mathbb{E}\{S(G, Y)\} \leq \mathbb{E}\{S(F, Y)\}$ when $Y \sim G$, i.e., on average, the true distribution G will not give a worse score than any other distribution F . Both of the scores that we consider, namely the squared error and Dawid–Sebastiani scores, are proper. Suppose that n_i is the observed number of firing events on segment i in the test set, with F_i^j the predictive distribution function for the number of firings, N_i^j , on this segment for model j , $1 \leq i \leq M, j \in \{\mathcal{M}_\Omega, \mathcal{M}_{\Omega, \mathcal{T}}, \mathcal{M}_{\Omega \times \Theta}, \mathcal{M}_{\Omega \times \Theta, \mathcal{T}}\}$, where M is the total number of segments in the test set. The number of firings, N_i^j , on segment i for model j , conditional on the latent parameters, is Poisson distributed with mean $\int_{\mathcal{T}} \lambda_{\mathcal{T}}(t) dt$, where \mathcal{T} is a time segment in the test set. The predictive probability mass function, f_i^j , for N_i^j is obtained by integrating out the latent parameters from the product of the Poisson distribution and the posterior of the latent parameters, which is an intractable integral. Although this Poisson mixture distribution for N_i^j is not available in closed form, its mean and variance may be obtained

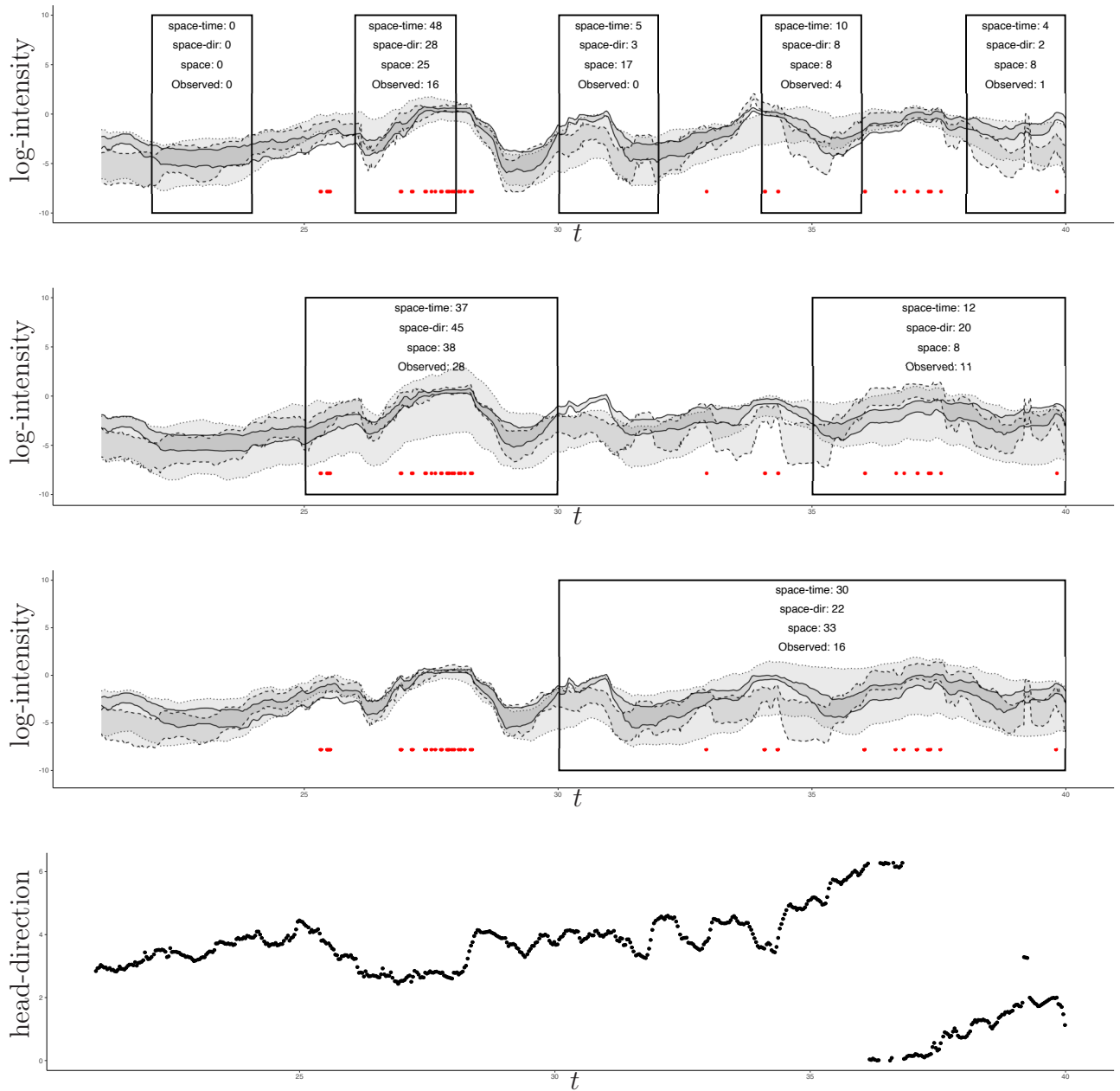


Figure 5: Illustration of output from cross-validation for models \mathcal{M}_Ω , $\mathcal{M}_{\Omega \times \Theta}$ and $\mathcal{M}_{\Omega, \mathcal{T}}$, for the time period 20–40 seconds, and for three time split sizes, first row: $\tau = 2\text{s}$, second row: $\tau = 5\text{s}$, third row: $\tau = 10\text{s}$. The last row shows the head-direction covariate over the same time period. Solid-lines, dashed-lines and dotted lines show point-wise 95% credible intervals of the logarithm of the intensity function $\lambda_{\mathcal{T}}(t)$ from models \mathcal{M}_Ω , $\mathcal{M}_{\Omega \times \Theta}$ and $\mathcal{M}_{\Omega, \mathcal{T}}$, respectively. The test set is the union of time intervals associated with the boxed regions. The training set is the complement of the test set. The statistics in the boxed regions show the mean of the posterior predictive distribution of the number of firings on the segment that each box corresponds to. The observed point pattern is superimposed on the first three panels and is shown with red dots.

		SE			DS		
split		$\mathcal{M}_{\Omega \times \Theta}$	$\mathcal{M}_{\Omega, \mathcal{T}}$	$\mathcal{M}_{\Omega \times \Theta, \mathcal{T}}$	$\mathcal{M}_{\Omega \times \Theta}$	$\mathcal{M}_{\Omega, \mathcal{T}}$	$\mathcal{M}_{\Omega \times \Theta, \mathcal{T}}$
Fold 1	2s	-24	76	139	-6	-8	-8
	5s	-65	1027	726	-9	-13	-13
	10s	-175	2767	2687	-15	-19	-20
	20s	-404	4643	2169	-8	-14	-15
	30s	-1520	1261	-862	-15	-26	-27
	40s	-1281	4183	272	-7	-8	-9
Fold 2	2s	-29	129	81	-8	-11	-9
	5s	-41	307	280	-22	-28	-29
	10s	-105	503	322	-14	-17	-17
	20s	-727	2452	2208	-29	-103	-99
	30s	-561	7020	1548	-9	-10	-12
	40s	-1817	9516	724	-21	-27	-28
Average	2s	-26	102	110	-7	-9	-8
	5s	-53	667	503	-16	-21	-21
	10s	-140	1635	1505	-14	-18	-18
	20s	-566	3548	2189	-19	-59	-57
	30s	-1041	4140	343	-12	-18	-19
	40s	-1549	6849	498	-14	-18	-19

Table 1: Average squared-error (SE) and Dawid–Sebastiani (DS) score difference between \mathcal{M} and \mathcal{M}_Ω for $\mathcal{M} \in \{\mathcal{M}_{\Omega \times \Theta}, \mathcal{M}_{\Omega, \mathcal{T}}, \mathcal{M}_{\Omega \times \Theta, \mathcal{T}}\}$, rounded to the nearest integer.

from the standard identities

$$\mathbb{E}(N_i^j) = \mathbb{E}\{\mathbb{E}(N_i^j \mid \mathbf{x}^j)\} \quad (8)$$

$$\text{var}(N_i^j) = \mathbb{E}\{\text{var}(N_i^j \mid \mathbf{x}^j)\} + \text{var}\{\mathbb{E}(N_i^j \mid \mathbf{x}^j)\} \quad (9)$$

where \mathbf{x}^j is the vector of latent parameters for model j , and the expectations are all conditional on the training set. We may obtain high precision estimates of (8) and (9) via Monte Carlo simulation. In particular, if $\mathbf{x}_1^j, \dots, \mathbf{x}_K^j$ are K independent realizations of the vector of latent parameters for model j , then we estimate $\mathbb{E}(N_i^j)$ using

$$\widehat{\mathbb{E}}(N_i^j) = \frac{1}{K} \sum_{k=1}^K \mathbb{E}(N_i^j \mid \mathbf{x}_k^j) \quad (10)$$

where $\mathbb{E}(N_i^j \mid \mathbf{x}_k^j)$ are obtained using the same numerical integration method as used in

Section 3.1. We estimate $\text{var}(N_i^j)$ using

$$\widehat{\text{var}}(N_i^j) = \frac{1}{K} \sum_{k=1}^K \mathbb{E}(N_i^j | \mathbf{x}_k^j) + \frac{1}{K} \sum_{k=1}^K \{\mathbb{E}(N_i^j | \mathbf{x}_k^j) - \widehat{\mathbb{E}}(N_i^j)\}^2 \quad (11)$$

where in the first sum we have used the fact that the conditional mean and variance of N_i^j given \mathbf{x}_k^j are equal since N_i^j given \mathbf{x}_k^j is Poisson distributed. In the `inlabru` package (Bachl et al., 2019), replications of the latent field can be obtained using the `generate` function.

We consider scoring rules that only depend on the mean and variance of the predictive distribution, as these are the only quantities that we easily have access to. In particular, we consider the squared error and Dawid–Sebastiani (Dawid and Sebastiani, 1999) scores, S_{SE} and S_{DS} respectively, defined by

$$S_{\text{SE}}(F_i^j, n_i) = (n_i - \mu_i^j)^2 \quad (12)$$

$$S_{\text{DS}}(F_i^j, n_i) = \left(\frac{n_i - \mu_i^j}{\sigma_i^j} \right)^2 + \log\{(\sigma_i^j)^2\} \quad (13)$$

where $\mu_i^j = \mathbb{E}(N_i^j)$ and $\sigma_i^j = \{\text{Var}(N_i^j)\}^{1/2}$ and $N_i^j \sim F_i^j$. As the exact values of μ_i^j and $(\sigma_i^j)^2$ are intractable, we replace them with their estimates from expressions (10) and (11).

To compare the predictive performance of models $\mathcal{M} \in \{\mathcal{M}_{\Omega \times \Theta}, \mathcal{M}_{\Omega, \mathcal{T}}, \mathcal{M}_{\Omega \times \Theta, \mathcal{T}}\}$ with the reference model \mathcal{M}_{Ω} , using a given score S that may be either S_{SE} or S_{DS} , we compute the set of model scores $\{S(F_i^{\mathcal{M}_{\Omega}}, n_i)\}_{i=1}^M$ and $\{S(F_i^{\mathcal{M}}, n_i)\}_{i=1}^M$ associated with models \mathcal{M}_{Ω} and \mathcal{M} , respectively. The model with lowest mean score is then preferred. To decide whether or not there is statistically significant evidence in favour of one model over the other we consider a hypothesis test with null hypothesis that the model scores $S(F_i^{\mathcal{M}}, n_i)$ and $S(F_i^{\mathcal{M}_{\Omega}}, n_i)$ are pairwise exchangeable for each $1 \leq i \leq M$, versus the alternative that \mathcal{M}_{Ω} is on average worse than \mathcal{M} . The test statistic T_{test} used for comparing between models \mathcal{M}_{Ω} and \mathcal{M} , is the observed mean difference in scores, with negative values indicating that the \mathcal{M} is better than the \mathcal{M}_{Ω} . Under the null hypothesis $S(F_i^{\mathcal{M}_{\Omega}}, n_i)$ and $S(F_i^{\mathcal{M}}, n_i)$ are

identically distributed, and so the observed score $S(F_i^{\mathcal{M}_\Omega}, n_i)$ would be equally likely to be produced by model \mathcal{M} , and similarly, $S(F_i^{\mathcal{M}}, n_i)$ is equally likely to be produced by \mathcal{M}_Ω . Thus, under the null hypothesis, for any given score difference $S_i^- = S(F_i^{\mathcal{M}}, n_i) - S(F_i^{\mathcal{M}_\Omega}, n_i)$, it would be equally likely that $-S_i^-$ was observed. This observation is used to construct a randomized testing procedure, given in Section 6.5 of the supplement, which allows us to approximate the distribution of T_{test} under the null hypothesis. The output of the test is an unbiased estimate of the one sided p -value for the test with null hypothesis that the scores $S(F_i^{\mathcal{M}_\Omega}, n_i)$ and $S(F_i^{\mathcal{M}}, n_i)$ are pairwise exchangeable for each $1 \leq i \leq M$. Small values of p give evidence against the null hypothesis in favour of \mathcal{M} . Conversely, values of p close to 1 give evidence against the null hypothesis in favour of \mathcal{M}_Ω . In our applications of Algorithm 1 we take $J = 10^6$.

		SE			DS		
interval		$\mathcal{M}_{\Omega \times \Theta}$	$\mathcal{M}_{\Omega, \mathcal{T}}$	$\mathcal{M}_{\Omega \times \Theta, \mathcal{T}}$	$\mathcal{M}_{\Omega \times \Theta}$	$\mathcal{M}_{\Omega, \mathcal{T}}$	$\mathcal{M}_{\Omega \times \Theta, \mathcal{T}}$
Fold 1	2s	0	0.96	0.96	0	0	0
	5s	0.02	1.00	0.92	0	0	0
	10s	0.07	1.00	1.00	0	0	0
	20s	0.05	1.00	0.89	0	0	0
	30s	0.05	0.83	0.11	0	0	0
	40s	0.01	1.00	0.63	0	0	0
Fold 2	2s	0	0.98	0.71	0	0	0
	5s	0.12	0.99	0.93	0	0	0
	10s	0.11	0.80	0.53	0	0	0
	20s	0.08	0.97	0.72	0	0	0
	30s	0.04	1.00	0.90	0	0.01	0
	40s	0.05	1.00	0.69	0	0	0
Folds combined	2s	0	1.00	0.96	0	0	0
	5s	0.01	1.00	0.98	0	0	0
	10s	0.02	1.00	0.99	0	0	0
	20s	0.01	1.00	0.91	0	0	0
	30s	0.01	1.00	0.65	0	0	0
	40s	0	1.00	0.72	0	0	0

Table 2: p -values of the hypothesis that the squared-error (DS) and Dawid–Sebastiani (DS) scores between model \mathcal{M} and \mathcal{M}_Ω , $\mathcal{M} \in \{\mathcal{M}_{\Omega \times \Theta}, \mathcal{M}_{\Omega, \mathcal{T}}, \mathcal{M}_{\Omega \times \Theta, \mathcal{T}}\}$, are pairwise exchangeable.

Figure 5 illustrates the design of the cross-validation scheme for a selection of models and interval sizes fitted to the spike-train data that we analyze in in Section 4.3. Table 1 shows

the average score differences for the two cross-validation folds, and their overall averages, for six interval sizes $\tau = 2\text{s}, 5\text{s}, 10\text{s}, 20\text{s}, 30\text{s},$ and 40s . The average SE score differences are all negative for $\mathcal{M}_{\Omega \times \Theta}$ and positive for $\mathcal{M}_{\Omega, \mathcal{T}}$ and $\mathcal{M}_{\Omega \times \Theta, \mathcal{T}}$, indicating that the temporally modulated models are, on average, less accurate in their predictions than \mathcal{M}_{Ω} . However, for the DS score differences, the values are negative for all three models, indicating that the additional model complexity provides a better match for the overall variability of the system, as the DS score takes into account both accuracy (bias) and precision (variability) of the predictions. These results are further confirmed by the p -values shown in Table 2. The proportions of negative score differences, shown in Section 6.4 of the supplement (Table 3), illustrate how often each model had a better score than the reference model \mathcal{M}_{Ω} , for SE and DS, respectively.

4.3 Analysis

Here, we analyze further the spike-train of $n = 6263$ firing events shown in Figure 1. We fit all models from Section 2.3 to the entire data set, using the values $\mu_{\Omega} = 20$, $\varsigma_{\Omega} = 0.4$, $a_{\Omega} = 2$, $b_{\Omega} = 20$, $\nu_{\Omega} = 1/2$, $\nu_{\Theta} = 1$, $\nu_{\mathcal{T}} = 1/3$, $\eta_{\Theta} = 1/(2\pi)$, and $\eta_{\mathcal{T}} = 1/100$, for the hyperparameters of the priors in Section 3.2.

Figure 9 shows the posterior mean and pointwise 95% credible intervals of $\xi_{\Omega}(s)$, $s \in \Omega$, for the baseline model \mathcal{M}_{Ω} and its temporally modulated version $\mathcal{M}_{\Omega, \mathcal{T}}$. The shape and the characteristics of the spatial effect overall agree between the two models, but there are key differences such as the smoothness and the uncertainty in the estimates, with $\mathcal{M}_{\Omega, \mathcal{T}}$ showing less uncertain and smoother estimates. This indicates that the inclusion of a temporally modulating factor captures overdispersion. Figure 9 shows the posterior mean of $\xi_{\Omega \times \Theta}(s, \theta)$ as a function of $s \in \Omega$ for a range of θ values from $\mathcal{M}_{\Omega \times \Theta}$ and $\mathcal{M}_{\Omega \times \Theta, \mathcal{T}}$. Pointwise 95% credible intervals are shown in Figures 13, 14, 15 and 16 of the supplement. Overall, the point and interval estimates agree between the two models, with the estimates

from $\mathcal{M}_{\Omega \times \Theta, \mathcal{T}}$ being smoother and less uncertain, which indicates again that the temporally modulated model $\mathcal{M}_{\Omega \times \Theta, \mathcal{T}}$ captures additional residual variability in the intensity of the spike train. Allowing for an interaction effect between space and head-direction shows that there is considerable variation in the locations of the peaks, and in the sizes and shapes of the fields locally at the peaks. Although the spatial effect is strongly oscillating, the posterior estimates do not rule out the possibility of ridges between the peaks, as for example, in the bottom left and right regions of Ω where there can be considerable intensity between fields of high intensity for certain θ values. Last, Figure 11 shows the posterior mean and

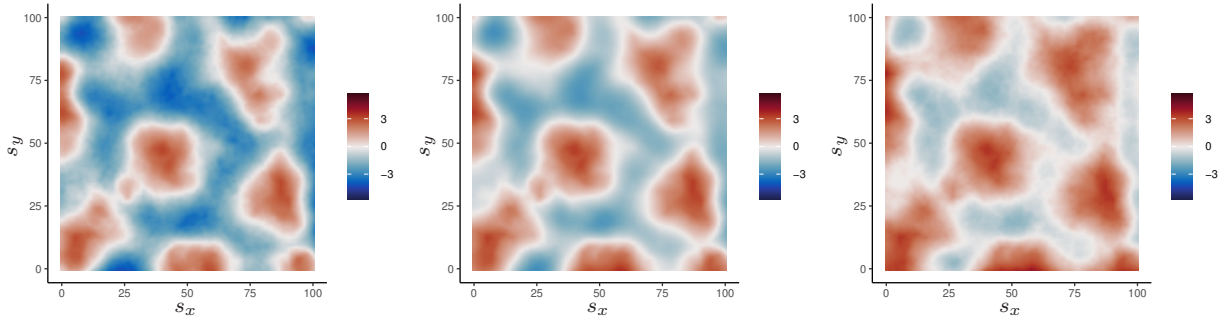


Figure 6: Posterior mean (center) and 95% credible intervals (left: 0.025 quantile, right: 0.975) of $\xi_{\Omega}\{(s_x, s_y)\}$ from \mathcal{M}_{Ω} .

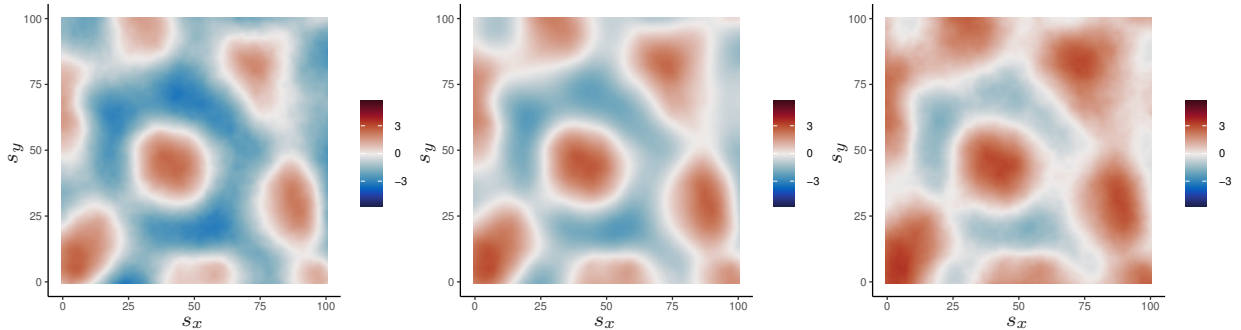


Figure 7: Posterior mean (center) and 95% credible intervals (left: 0.025 quantile, right: 0.975) of $\xi_{\Omega}\{(s_x, s_y)\}$ from $\mathcal{M}_{\Omega, \mathcal{T}}$.

95% credible intervals of $\xi_{\Omega \times \Theta}(s, \theta)$ as a function of $\theta \in \mathbb{S}_1$ for a range of s values from $\mathcal{M}_{\Omega \times \Theta}$ and $\mathcal{M}_{\Omega \times \Theta, \mathcal{T}}$. The shape of the head-directional effect also varies with location, and is more prominent in regions where the spatial effect is low and less so in regions where the spatial effect is high. This is also confirmed from Figure 12 which shows the posterior mean

and 95% credible intervals of the temporally modulating component $\xi_{\mathcal{T}}(t)$ for a range of t values from $\mathcal{M}_{\Omega, \mathcal{T}}$ and $\mathcal{M}_{\Omega \times \Theta, \mathcal{T}}$. The scatterplot shows that for the temporally modulated models, the additional inclusion of a directional effect shifts the posterior distribution of $\xi_{\mathcal{T}}$. When the modulating effect $\xi_{\mathcal{T}}$ is low, then on average, the posterior mean from $\mathcal{M}_{\Omega \times \Theta, \mathcal{T}}$ is larger than the posterior mean from $\mathcal{M}_{\Omega \times \Theta}$ and vice versa.

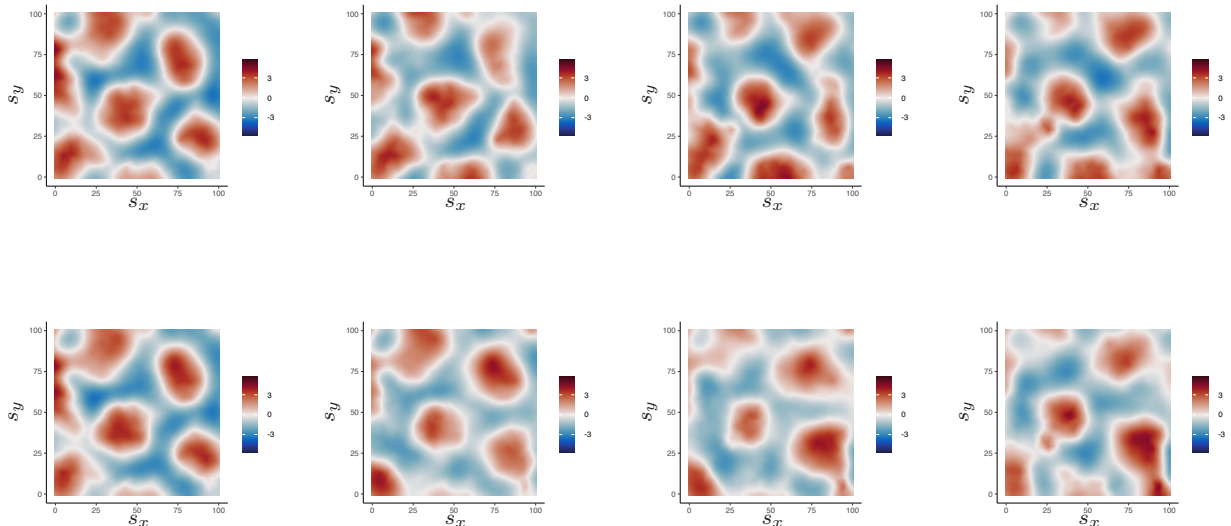


Figure 8: Posterior mean of $\xi_{\Omega \times \Theta}\{(s_x, s_y), \theta\}$ from $\mathcal{M}_{\Omega \times \Theta}$, shown in clockwise order for a sequence of equally spaced θ values ranging from $\pi/8$ (top left) to 2π (bottom left).

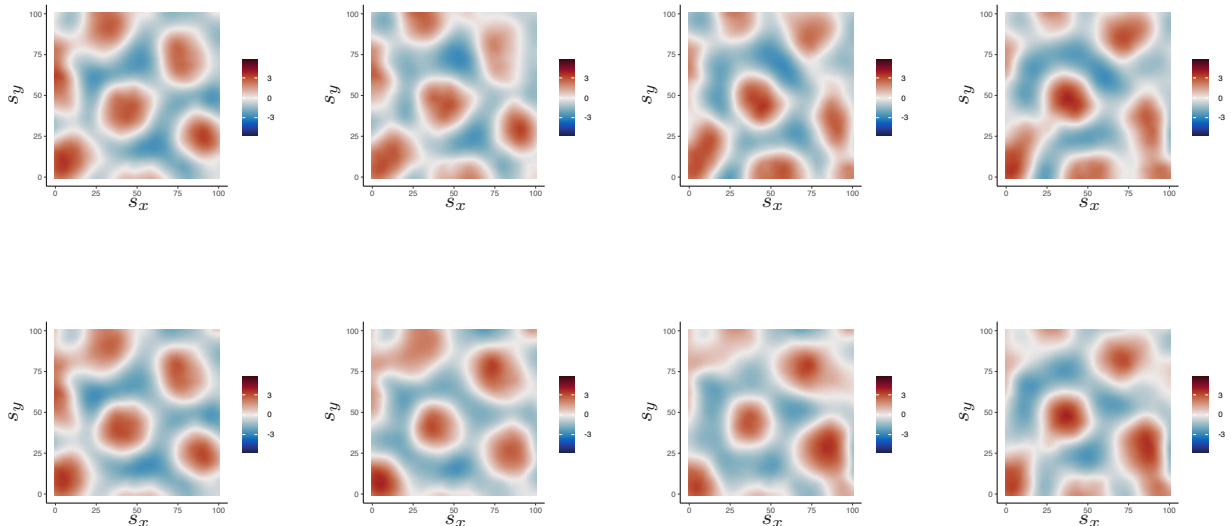


Figure 9: Posterior mean of $\xi_{\Omega \times \Theta}\{(s_x, s_y), \theta\}$ from $\mathcal{M}_{\Omega \times \Theta, \mathcal{T}}$, shown in clockwise order for a sequence of equally spaced θ values ranging from $\pi/8$ (top left) to 2π (bottom left).

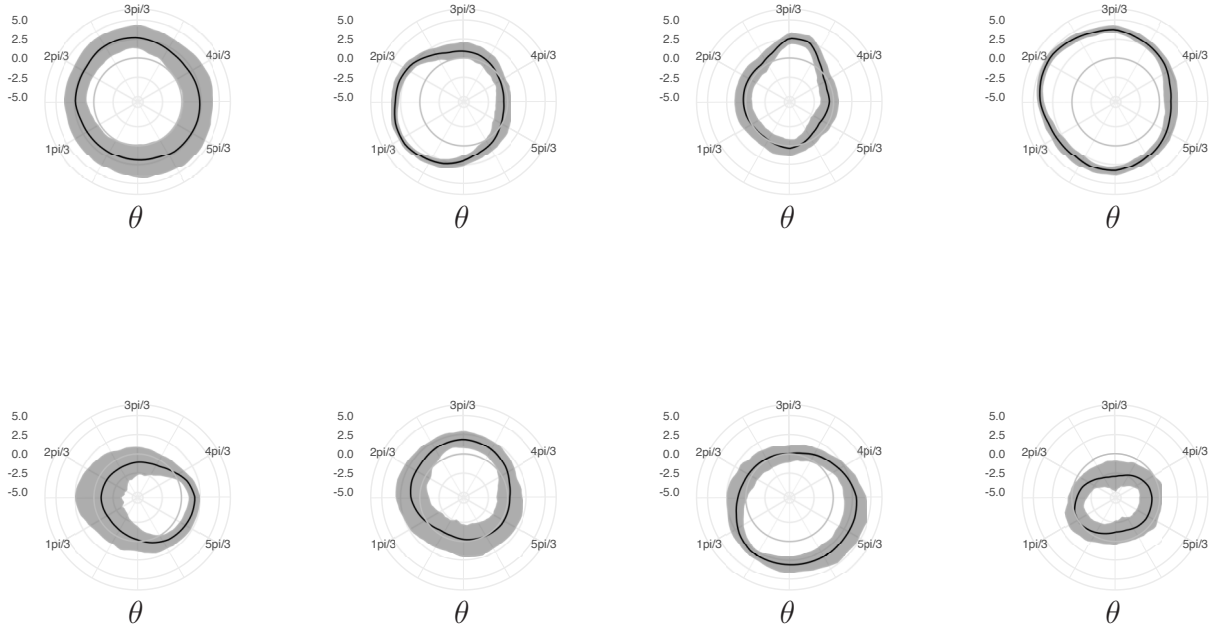


Figure 10: Posterior mean (solid black) and pointwise 95% credible intervals (grey ribbon) of $\xi_{\Omega \times \Theta} \{(s_x, s_y), \theta\}$ from $\mathcal{M}_{\Omega \times \Theta}$, shown in clockwise order for a sequence of equally spaced values of (s_x, s_y) on the diagonal ranging from $(s_x, s_y) = (0, 0)$ to $(s_x, s_y) = (100, 100)$. The circle shown in dark grey shows the constant function which is equal to zero.

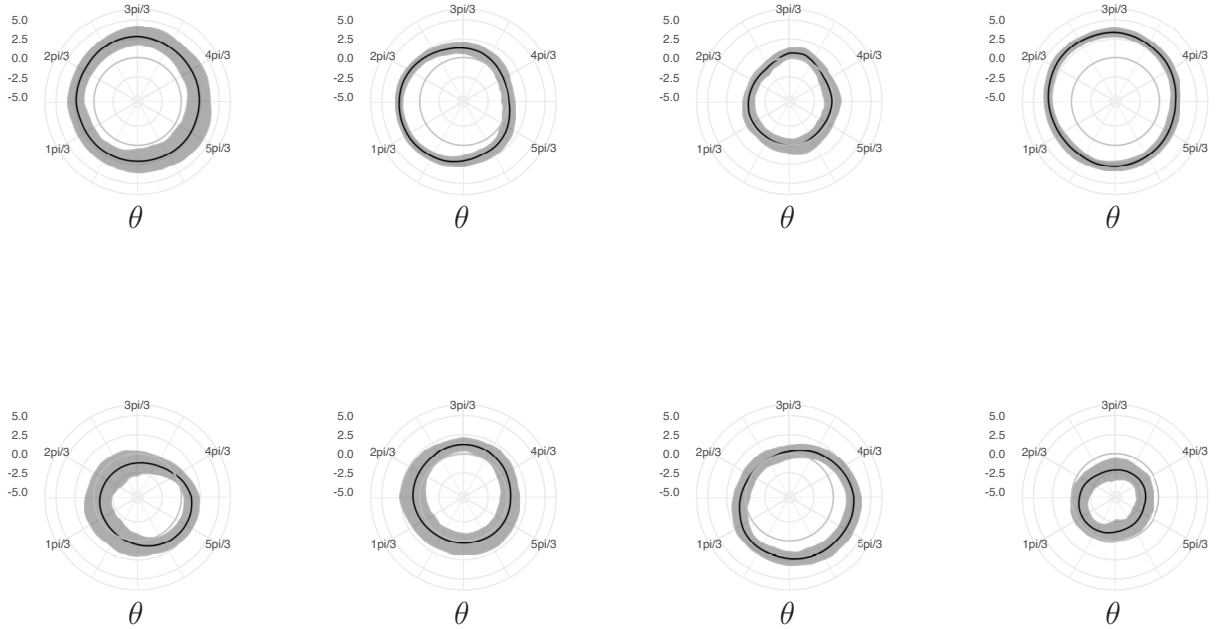


Figure 11: Posterior mean (solid black) and pointwise 95% credible intervals (grey ribbon) of $\xi_{\Omega \times \Theta} \{(s_x, s_y), \theta\}$ from $\mathcal{M}_{\Omega \times \Theta, \tau}$, shown in clockwise order for a sequence of equally spaced values of (s_x, s_y) on the diagonal ranging from $(s_x, s_y) = (0, 0)$ to $(s_x, s_y) = (100, 100)$. The circle shown in dark grey shows the constant function which is equal to zero.

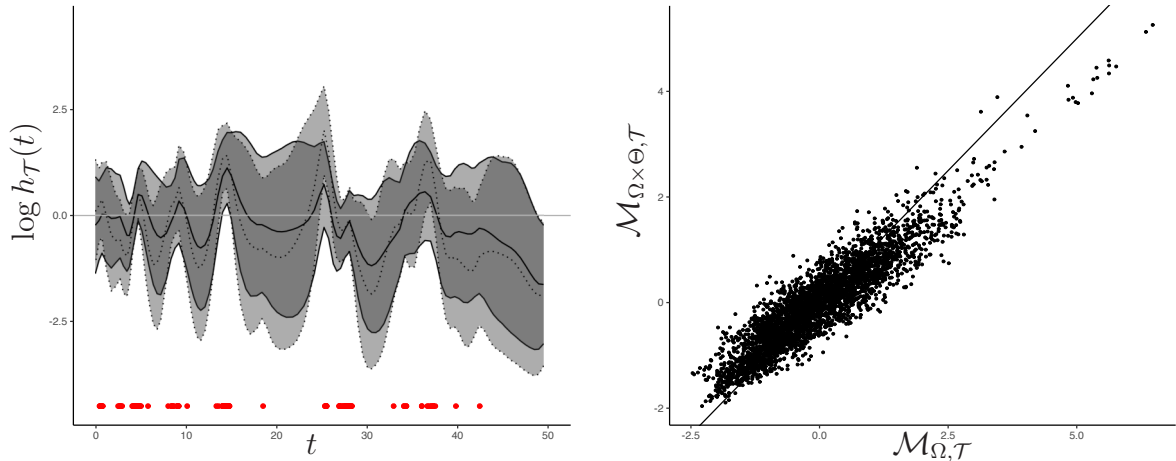


Figure 12: *Left*: Posterior mean and pointwise 95% credible intervals of $\xi_{\mathcal{T}}(t)$ from $\mathcal{M}_{\Omega, \mathcal{T}}$ (dotted) and $\mathcal{M}_{\Omega \times \Theta, \mathcal{T}}$ (solid) plotted over the time interval 0–50 seconds. *Right*: scatterplot of posterior mean values of $\xi_{\mathcal{T}}(t)$ from $\mathcal{M}_{\Omega, \mathcal{T}}$ and $\mathcal{M}_{\Omega \times \Theta, \mathcal{T}}$ at the nodes of the temporal mesh, which covers the entire interval of the experiment.

5 Discussion

We introduce a novel and principled framework for analysis of neural representations of space. We developed new statistical models, based on Cox processes, that are amenable to modelling the relationship between neural activity and covariates, including time, space and other covariates such as head direction. Our approach rests on modelling firing activity using Poisson point processes with latent Gaussian effects. Our analyses in Sections 4.2 and 4.3 demonstrate that our proposed models have better predictive performance than currently widely used models (e.g. [Sargolini et al. \(2006\)](#)). The latent prior Gaussian effects accommodate persistent inhomogeneous spatial-directional patterns and overdispersion. Inference was performed in a fully Bayesian manner, which allowed us to quantify uncertainty and to identify effects that are typically missed out from most previous analyses. Our approach supersedes a recently introduced framework that uses Poisson generalised linear models with latent effects to model grid cell activity ([Rule et al. \(2023\)](#)): it does not involve binning of data; incorporates more flexible priors that are quasi-oscillatory; accommodates local distortions; by design does not assume long-range dependence; and

enables modelling of the effect of covariates without the risk of ecological bias. While our focus here is on the development and validation of the modelling framework, it could be extended to generate metrics of grid field properties from the model fitting hyper-parameters and statistical models for the effects of experimental manipulations, e.g. effects of objects and environmental geometry.

Declaration

All animal procedures were performed under a UK Home Office licence (PC198F2A0) in accordance with The University of Edinburgh Animal Welfare committee’s guidelines. All procedures complied with the Animals (Scientific Procedures) Act, 1986, and were approved by a named Veterinary Surgeon and local ethical review committee.

6 Supplementary material

6.1 R code and data set

GitHub repository: Repository containing R code to perform model fitting of the models described in the article:

https://github.com/ipapasta/grid_fields

Grid cells data set: Data set used in the analysis of our statistical methods in Section 4:

<https://datashare.ed.ac.uk/handle/10283/3674>

6.2 Covariance of cyclic Matérn process

Proof of Proposition 1. For a regular mesh $0 = k_0 < \dots < k_{p-1} < k_p = 2\pi$ on Θ with $k_i - k_{i-1} = h$, for all $i = 1, \dots, p$, we have that $\kappa^2 C + G = \text{circulant}(\kappa^2 h + (2/h), -1/h, 0, \dots, 0, -1/h)$. The elements of the inverse of a circulant matrix having only three non-zero elements in each row can be derived analytically from the solution of a recurrence equation (Searle, 1979), not least, we

have that $(\kappa^2 C + G)^{-1} = \text{circulant}(a_0, a_1, \dots, a_{p-1})$, where

$$a_j = \frac{z_1 z_2}{(-1/h)(z_1 - z_2)} \left(\frac{z_1^j}{1 - z_1^p} - \frac{z_2^j}{1 - z_2^p} \right), \quad j = 0, \dots, p-1$$

with

$$z_1 = \frac{-\kappa^2 h - (2/h) + (\kappa^2 h^2 + 4\kappa^2)^{1/2}}{-2/h} \quad \text{and} \quad z_2 = \frac{\kappa^2 h + (2/h) + (\kappa^2 h^2 + 4\kappa^2)^{1/2}}{2/h}.$$

Let $\theta = 2\pi j/p \in \Theta$. Then, as $p \rightarrow \infty$ and $h \rightarrow 0$, the covariance function $r(\theta) = a_{p\theta/(2\pi)}$ of the limiting process converges to

$$r(\theta) \rightarrow \frac{1}{2\kappa} \frac{\cosh\{(\pi - \theta)\kappa\}}{\sinh(\pi\kappa)} \quad \text{as } p \rightarrow \infty,$$

The case $\alpha = 2$ is obtained by direct convolution of the covariance function associated with $\alpha = 1$ (Lindgren et al., 2011), that is,

$$\frac{1}{(2\kappa)^2 \sinh(\pi\kappa)} \int_0^{2\pi} \cosh\{(\pi - |u|)\kappa\} \cosh\{(\pi - |\theta - u|)\kappa\} du =: \zeta_{\Theta}(\theta).$$

□

6.3 Variances of Gaussian random fields

Proof of Proposition 2. Explicit expressions for the variance for the case where $\phi_{\Omega} \in (-1, 1]$ are derived and documented in Lindgren et al. (2011). Thus, we proceed by deriving the variance of the stationary Gaussian random field for the overdamped case, that is, when $\phi_{\Omega} > 1$. Dropping the manifold index from the parameters, we have that for $\phi > 1$, direct computation of the variance from the spectral density, after a change from Cartesian to polar coordinates (Lindgren, 2012), is

equal to to

$$\begin{aligned}
\text{var}\{\xi_\Omega(s)\} &= (2\pi) \int_0^\infty \frac{r}{(2\pi)^2 \kappa^4 + 2\kappa^2 \phi r^2 + r^4} \frac{\sigma^2}{r} dr = \frac{\sigma^2}{4\pi} \int_0^\infty \frac{du}{\kappa^4 + 2\kappa^2 \phi u + u^2} = \\
&= \frac{\sigma^2}{4\pi} \int_0^\infty \frac{du}{(u + \kappa^2 \phi)^2 + \kappa^4 - \kappa^4 \phi^2} = \frac{\sigma^2}{4\pi} \int_{\frac{\phi}{\sqrt{\phi^2-1}}}^\infty \frac{dv}{(\kappa^4 \phi^2 - \kappa^2)v^2 - (\kappa^4 \phi^2 - \kappa^2)} = \\
&= \frac{\sigma^2}{(4\pi)\sqrt{\kappa^4 \phi^2 - \kappa^4}} \int_{\frac{\phi}{\sqrt{\phi^2-1}}}^\infty (v^2 - 1)^{-1} dv = \\
&= \frac{\sigma^2}{(4\pi)\sqrt{\kappa^4 \phi^2 - \kappa^4}} \left[\frac{\iota\pi}{2} \lim_{v \rightarrow \infty} \{\log(1+v) - \log(v-1)\} + \frac{1}{2} \log \left(1 + \frac{\phi}{\sqrt{\phi^2-1}} \right) - \right. \\
&\quad \left. - \frac{\iota\pi}{2} - \frac{1}{2} \log \left(\frac{\phi}{\sqrt{\phi^2-1}} - 1 \right) \right] \\
&= \frac{\sigma^2}{4\pi\kappa^2\sqrt{\varphi^2-1}} \left\{ \frac{\pi}{2} - \text{atan}\{(\varphi^2-1)^{-1/2}\varphi\} \right\}
\end{aligned}$$

□

Proof of Proposition 3. Dropping the manifold index from the parameters, direct calculation of the variance from the spectral mass function gives that

$$\text{var}\{\xi_\Theta(\theta)\} = \sum_{\omega \in \mathbb{Z}} f_\theta(\omega) = \frac{\sigma^2 \pi \kappa}{4\kappa^3 (\varphi^2 - 1)^{1/2}} \left(\frac{\cot(iz)}{iz} - \frac{\cot(i\bar{z})}{i\bar{z}} \right), \quad \varphi \in (-1, \infty), \quad (14)$$

where $\bar{z} = \pi\kappa(\varphi + (1 - \varphi^2)^{1/2}i)^{1/2}$. When $\varphi \in [1, \infty)$, $iz \in \mathbb{R}$ is real and expression (14) gives the variance that is stated in the proposition.

For $\varphi \in (-1, 1)$ we use the trigonometric identity $\cot(iA)/iA = -\coth(A)/A$ for any $A \in \mathbb{C}$, to rewrite expression (14) as

$$\text{var}\{\xi_\Theta(\theta)\} = \frac{\sigma^2 \pi \kappa}{4\kappa^3 (1 - \varphi^2)^{1/2} i} \left(\frac{\coth(\bar{z})}{\bar{z}} - \frac{\coth(z)}{z} \right),$$

which, upon further simplification based on the identity

$$\frac{\coth(x + iy)}{x + iy} - \frac{\coth(x - iy)}{x - iy} \frac{2i}{(x^2 + y^2)} = \frac{x \sin(2y) + y \sinh(2x)}{\cos(2y) - \cosh(2x)}, \quad x, y \in \mathbb{R},$$

proves the claim for the underdamped case. \square

Proof of Proposition 4. Dropping the manifold index from the parameters, for $-1 < \varphi < 1$, $\text{var}\{\xi_{\mathcal{T}}(t)\}$ is equal to

$$\begin{aligned} \int_{-\infty}^{\infty} S(\omega; \kappa, \varphi) d\omega &= \frac{1}{\pi} \int_0^{\infty} \frac{1}{\kappa^4 + 2\varphi\kappa^2\omega^2 + \omega^4} d\omega \\ &= \frac{1}{\pi} \int_0^{\infty} \frac{\kappa}{2\sqrt{u}} \frac{du}{\kappa^4 + 2\varphi\kappa^4u + \kappa^4u^2} = \frac{1}{2\pi\kappa^3} \int_0^{\infty} \frac{du}{\sqrt{u}} \frac{1}{1 + 2\varphi u + u^2} \\ &= \frac{1}{2\pi\kappa^3} 2^{1/2}(1 - \varphi^2)^{-1/4} \Gamma(3/2) B(1/2, 3/2) P_{-1}^{-1/2}(\varphi) \end{aligned}$$

where the last expression follows after using [Gradshteyn and Ryzhik](#) (expression 3.252.10 in [2014](#)) with $\mu = 1/2$, $\nu = 1$, and $\cos(t) = \varphi$, so that $\sin(t) = \sqrt{1 - \varphi^2}$. Note that $\Gamma(3/2) = \sqrt{\pi}/2$ and $B(1/2, 3/2) = \pi/2$. Hence, using the sin-half-angle formula (expression 8.754 in [Gradshteyn and Ryzhik, 2014](#)) we have that

$$\begin{aligned} \text{var}\{\xi_{\mathcal{T}}(t)\} &= \frac{\pi^{1/2}}{2^{5/2}\kappa^3} (1 - \varphi^2)^{-1/4} P_{-1}^{-1/2}(\varphi) = \frac{\pi^{1/2}}{2^{5/2}\kappa^3} (1 - \varphi^2)^{-1/4} \sqrt{\frac{2}{\pi\sqrt{1 - \varphi^2}}} \frac{\sqrt{(1 - \varphi)/2}}{1/2} \\ &= \frac{2}{2^{5/2}\kappa^3} \sqrt{\frac{1 - \varphi}{1 - \varphi^2}} = \frac{1}{4\kappa^3} \sqrt{\frac{2}{1 + \varphi}}. \end{aligned}$$

Now, consider the case $\varphi > 1$. We have

$$\begin{aligned} \text{var}\{\xi_{\mathcal{T}}(t)\} &= \frac{1}{2\pi} \int_{-\infty}^{\infty} \frac{d\omega}{\kappa^4 + 2\varphi\kappa^2\omega^2 + \omega^4} = \frac{\kappa}{2\pi} \int_0^{\infty} \frac{du}{\kappa^4 + 2\varphi\kappa^4u^2 + \kappa^4u^4} \\ &= \frac{1}{2\pi\kappa^3} \int_{-\infty}^{\infty} \frac{du}{1 + 2\varphi u^2 + u^4} = \frac{1}{2\pi\kappa^3} \int_{-\infty}^{\infty} \frac{du}{2\sqrt{\varphi^2 - 1}} \left(\frac{1}{u^2 + \varphi - \sqrt{\varphi^2 - 1}} - \frac{1}{u^2 + \varphi + \sqrt{\varphi^2 - 1}} \right) \end{aligned}$$

where the last step is obtained via the polynomial roots $a_{\pm} = -\varphi \pm \sqrt{\varphi^2 - 1} < 0$ (with respect

to u^2).

Next, we have that $\text{var}\{\xi_{\mathcal{T}}(t)\}$ is equal to

$$\begin{aligned} & \frac{1}{4\pi\kappa^3\sqrt{\varphi^2-1}} \left(\int_{-\infty}^{\infty} \frac{du}{u^2-a_+} - \int_{-\infty}^{\infty} \frac{du}{u^2-a_-} \right) = \frac{1}{4\pi\kappa^3\sqrt{\varphi^2-1}} \left(\int_{-\infty}^{\infty} \frac{\sqrt{-a_+} dv}{-v^2a_+ - a_+} - \int_{-\infty}^{\infty} \frac{\sqrt{-a_-} dv}{-v^2a_- - a_-} \right) \\ &= \frac{1}{4\pi\kappa^3\sqrt{\varphi^2-1}} \left(\frac{\sqrt{-a_+}}{-a_+} - \frac{\sqrt{-a_-}}{-a_-} \right) \int_{-\infty}^{\infty} \frac{dv}{v^2+1} = \frac{1}{4\pi\kappa^3\sqrt{\varphi^2-1}} \left(\frac{1}{\sqrt{-a_+}} - \frac{1}{\sqrt{-a_-}} \right) [\arctan(v)]_{v=-\infty}^{\infty} \\ &= \frac{1}{4\kappa^3\sqrt{\varphi+1}\sqrt{\varphi-1}} \left(\frac{1}{\sqrt{\varphi-\sqrt{\varphi^2-1}}} - \frac{1}{\sqrt{\varphi+\sqrt{\varphi^2-1}}} \right). \end{aligned}$$

Let $b_+ = -a_-$ and $b_- = -a_+$. Then, using that $b_- + b_+ = \varphi - \sqrt{\varphi^2-1} + \varphi + \sqrt{\varphi^2-1} = 2\varphi$ and $b_-b_+ = (\varphi - \sqrt{\varphi^2-1})(\varphi + \sqrt{\varphi^2-1}) = \varphi^2 - \varphi^2 + 1 = 1$,

$$\begin{aligned} \text{var}\{\xi_{\mathcal{T}}(t)\} &= \frac{1}{4\kappa^3\sqrt{\varphi+1}} \sqrt{\frac{2}{b_+ + b_- - 2\sqrt{b_-b_+}}} \left(\frac{1}{\sqrt{b_-}} - \frac{1}{\sqrt{b_+}} \right) \\ &= \frac{1}{4\kappa^3} \sqrt{\frac{2}{\varphi+1}} \sqrt{\frac{1}{(\sqrt{b_+} - \sqrt{b_-})^2}} \frac{\sqrt{b_+} - \sqrt{b_-}}{\sqrt{b_+b_-}} = \frac{1}{4\kappa^3} \sqrt{\frac{2}{\varphi+1}}. \end{aligned}$$

□

6.4 Additional Tables and Figures

In this section, we provide additional Tables and Figures that are referenced in the main text. Table 3 shows the proportions of negative score differences between models \mathcal{M} and \mathcal{M}_{Ω} . Figure 4 shows conservative estimates of the standard deviation of squared-error score differences between model \mathcal{M} and model \mathcal{M}_{Ω} . Figures 13, 14, 15 and 16 show pointwise 95% credible intervals of $\xi_{\Omega \times \Theta}(s, \theta)$ for models $\mathcal{M}_{\Omega \times \Theta}$ and $\mathcal{M}_{\Omega \times \Theta, \mathcal{T}}$.

6.5 Permutation test

		SE			DS		
interval		$\mathcal{M}_{\Omega \times \Theta}$	$\mathcal{M}_{\Omega, \mathcal{T}}$	$\mathcal{M}_{\Omega \times \Theta, \mathcal{T}}$	$\mathcal{M}_{\Omega \times \Theta}$	$\mathcal{M}_{\Omega, \mathcal{T}}$	$\mathcal{M}_{\Omega \times \Theta, \mathcal{T}}$
Fold 1	2s	0.61	0.57	0.58	0.60	0.52	0.55
	5s	0.53	0.44	0.51	0.56	0.46	0.50
	10s	0.57	0.30	0.33	0.66	0.58	0.62
	20s	0.64	0.25	0.48	0.64	0.64	0.66
	30s	0.69	0.52	0.59	0.76	0.76	0.83
	40s	0.73	0.18	0.50	0.73	0.68	0.68
Fold 2	2s	0.58	0.51	0.58	0.59	0.54	0.57
	5s	0.56	0.47	0.50	0.61	0.53	0.56
	10s	0.57	0.39	0.54	0.61	0.51	0.56
	20s	0.69	0.40	0.51	0.76	0.64	0.67
	30s	0.57	0.20	0.40	0.60	0.50	0.53
	40s	0.65	0.30	0.48	0.83	0.78	0.83
Folds combined	2s	0.59	0.54	0.58	0.59	0.53	0.56
	5s	0.55	0.45	0.51	0.59	0.50	0.53
	10s	0.57	0.34	0.44	0.63	0.54	0.59
	20s	0.66	0.33	0.49	0.70	0.64	0.66
	30s	0.63	0.36	0.49	0.68	0.63	0.68
	40s	0.69	0.24	0.49	0.78	0.73	0.76

Table 3: Proportion of negative squared-error (SE) and Dawid–Sebastiani (DS) score differences between model \mathcal{M} and \mathcal{M}_{Ω} , for $\mathcal{M} \in \{\mathcal{M}_{\Omega \times \Theta}, \mathcal{M}_{\Omega, \mathcal{T}}, \mathcal{M}_{\Omega \times \Theta, \mathcal{T}}\}$.

		SE			DS		
interval		$\mathcal{M}_{\Omega \times \Theta}$	$\mathcal{M}_{\Omega, \mathcal{T}}$	$\mathcal{M}_{\Omega \times \Theta, \mathcal{T}}$	$\mathcal{M}_{\Omega \times \Theta}$	$\mathcal{M}_{\Omega, \mathcal{T}}$	$\mathcal{M}_{\Omega \times \Theta, \mathcal{T}}$
Fold 1	2s	160	903	1886	39.6	52.4	51.9
	5s	454	8339	8502	31.0	58.5	57.8
	10s	1168	11147	17520	80.4	97.4	98.2
	20s	1594	12504	12457	19.8	48.7	48.0
	30s	4926	6444	3655	26.8	41.6	40.9
	40s	2582	10903	3744	9.6	11.7	11.7
Fold 2	2s	238	1828	1846	54.7	63.2	65.8
	5s	452	2490	2822	192.5	247.9	248.7
	10s	793	4621	4513	76.2	81.5	69.6
	20s	3423	10408	15885	113.9	583.5	551.6
	30s	1728	12957	6586	19.7	25.6	25.3
	40s	5292	16016	6953	48.3	56.1	55.8
Average	2s	199	1366	1866	47.2	57.8	58.8
	5s	453	5414	5662	111.8	153.2	153.3
	10s	980	7884	11016	78.3	89.5	83.9
	20s	2508	11456	14171	66.9	316.1	299.8
	30s	3327	9700	5120	23.3	33.6	33.1
	40s	3937	13460	5348	29.0	33.9	33.7

Table 4: Conservative estimates of standard deviation of squared-error (SE) and Dawid–Sebastiani (DS) score differences between model \mathcal{M} and model \mathcal{M}_{Ω} with $\mathcal{M} \in \{\mathcal{M}_{\Omega \times \Theta}, \mathcal{M}_{\Omega, \mathcal{T}}, \mathcal{M}_{\Omega \times \Theta, \mathcal{T}}\}$, rounded to the nearest integer.

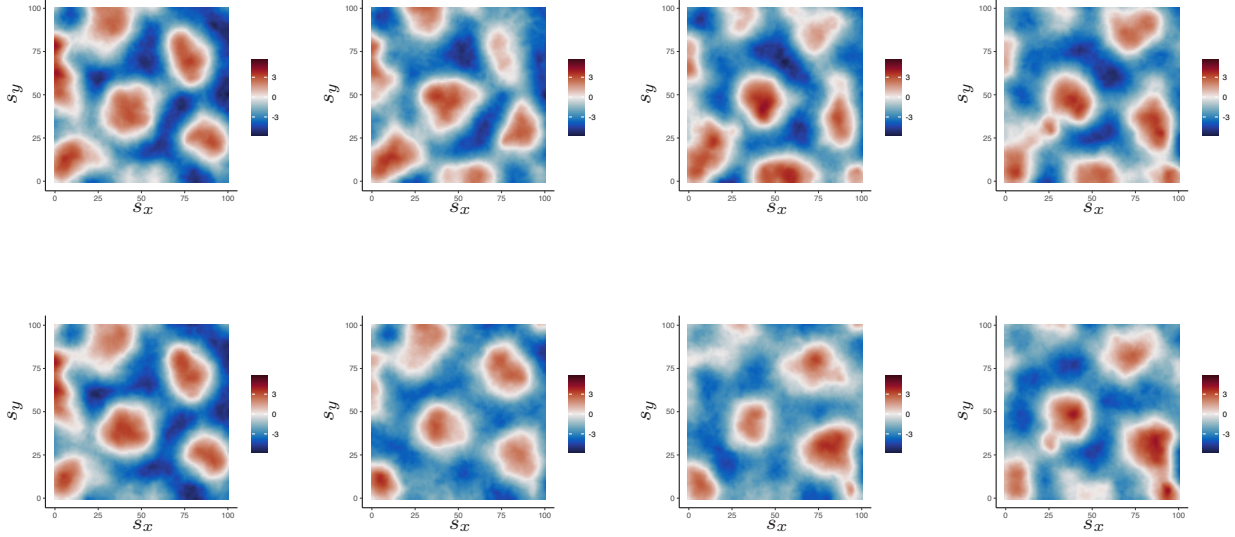


Figure 13: Posterior 0.025 quantile of $\xi_{\Omega \times \Theta}((s_x, s_y), \theta)$ from $\mathcal{M}_{\Omega \times \Theta}$, shown in clockwise order for a sequence of equally spaced θ values ranging from $\pi/8$ (top left) to 2π (bottom left).

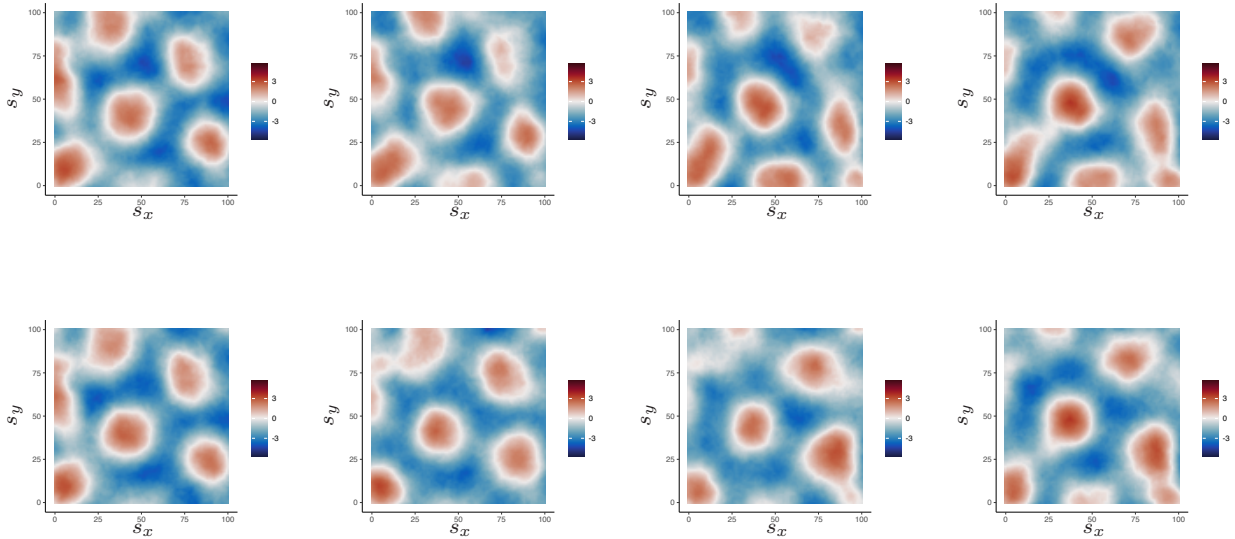


Figure 14: Posterior 0.025 quantile of $\xi_{\Omega \times \Theta}((s_x, s_y), \theta)$ from $\mathcal{M}_{\Omega \times \Theta, \mathcal{T}}$, shown in clockwise order for a sequence of equally spaced θ values ranging from $\pi/8$ (top left) to 2π (bottom left).

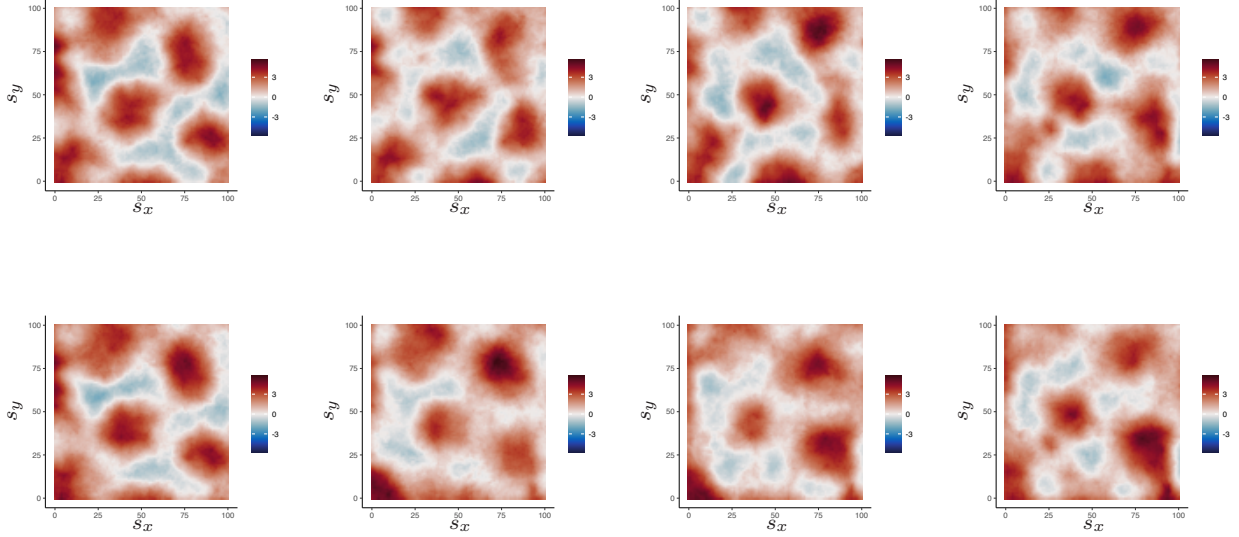


Figure 15: Posterior 0.975 quantile of $\xi_{\Omega \times \Theta}((s_x, s_y), \theta)$ from $\mathcal{M}_{\Omega \times \Theta}$, shown in clockwise order for a sequence of equally spaced θ values ranging from $\pi/8$ (top left) to 2π (bottom left).

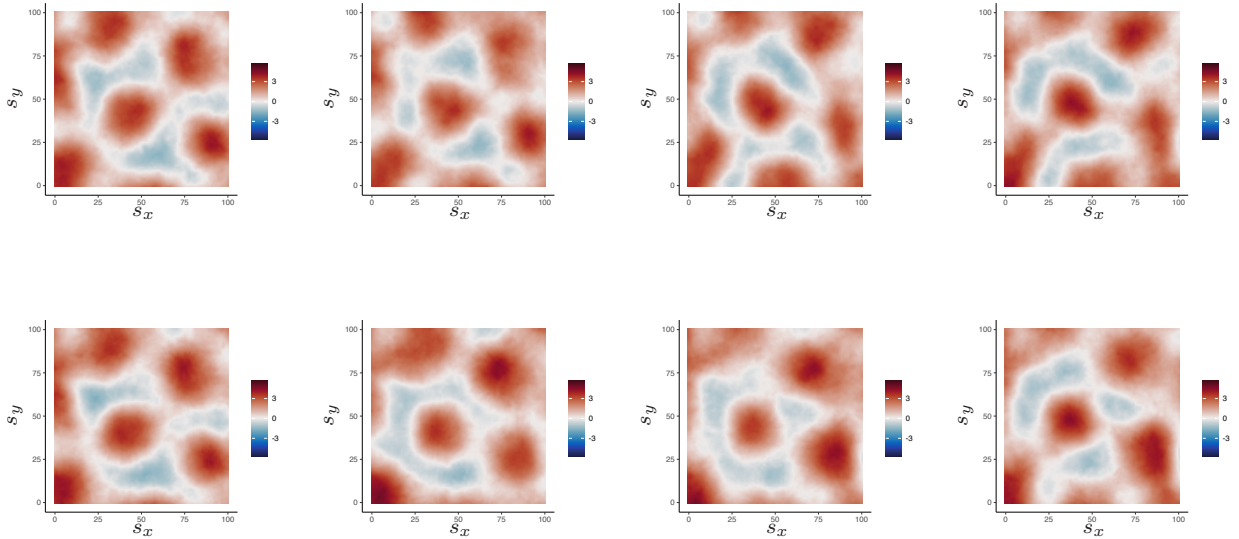


Figure 16: Posterior 0.975 quantile of $\xi_{\Omega \times \Theta}((s_x, s_y), \theta)$ from $\mathcal{M}_{\Omega \times \Theta, \mathcal{T}}$, shown in clockwise order for a sequence of equally spaced θ values ranging from $\pi/8$ (top left) to 2π (bottom left).

```

input :  $J \in \mathbb{N}$  and negatively oriented model scores  $S(F_i^{\mathcal{M}}, n_i), S(F_i^{\mathcal{M}_\Omega}, n_i)$ ,
           $1 \leq i \leq N_{\text{val}}$ .
output:  $p$ , an estimate of the  $p$ -value of the test.
1 for  $i \leftarrow 1$  to  $N_{\text{val}}$  do
2   |   compute the score difference;
3   |    $S_i^- = S(F_i^{\mathcal{M}}, n_i) - S(F_i^{\mathcal{M}_\Omega}, n_i)$  ;
4 end
5 compute the observed test statistic  $T_{\text{obs}} = \frac{1}{N_{\text{val}}} \sum_{i=1}^{N_{\text{val}}} S_i^-$  ;
6 for  $j \leftarrow 1$  to  $J$  do
7   |   for  $i \leftarrow 1$  to  $N_{\text{val}}$  do
8     |   compute the randomized score difference;
9     |
10    |   
$$S_i^-(j) = \begin{cases} S_i^- & \text{with probability } 0.5 \\ -S_i^- & \text{with probability } 0.5 \end{cases}$$

11   |   end
12   |   compute  $T_j = \frac{1}{N_{\text{val}}} \sum_{i=1}^{N_{\text{val}}} S_i^-(j)$  ;
13 end
14 return  $p = \frac{1}{J} \sum_{j=1}^J \mathbb{1}[T_j \leq T_{\text{obs}}]$ .

```

Algorithm 1: Hypothesis testing procedure for testing pairwise exchangeability of model scores. The computed p -value is close to zero if model \mathcal{M} is better than model \mathcal{M}_Ω , and close to 1 if model \mathcal{M}_Ω is better. A two-sided test p -value can be obtained as $2 \min(p, 1 - p)$. The positive integer N_{val} corresponds to the number of connected segments on the mouses trajectory in the validation set.

References

- Adler, R. J. and Taylor, J. E. (2007), *Random Fields and Geometry*, Vol. 80, Springer.
- Bachl, F. E., Lindgren, F., Borchers, D. L. and Illian, J. B. (2019), ‘inlabru: an R package for Bayesian spatial modelling from ecological survey data’, *Methods in Ecology and Evolution* **10**, 760–766.
- Chung, J. E., Magland, J. F., Barnett, A. H., Tolosa, V. M., Tooker, A. C., Lee, K. Y., Shah, K. G., Felix, S. H., Frank, L. M. and Greengard, L. F. (2017), ‘A fully automated approach to spike sorting’, *Neuron* **95**, 1381–1394.
- Dawid, A. P. and Sebastiani, P. (1999), ‘Coherent dispersion criteria for optimal experimental design’, *Annals of Statistics* pp. 65–81.
- Dayan, P. and Abbott, L. F. (2005), *Theoretical Neuroscience: Computational and Mathematical Modeling of Neural Systems*, MIT Press.
- Diggle, P. (1985), ‘A kernel method for smoothing point process data’, *Journal of the Royal Statistical Society: Series C (Applied Statistics)* **34**, 138–147.
- Eichenbaum, H. and Lipton, P. A. (2008), ‘Towards a functional organization of the medial temporal lobe memory system: Role of the parahippocampal and medial entorhinal cortical areas’, *Hippocampus* **18**, 1314–1324.
- Gerlei, K., Passlack, J., Hawes, I., Vandrey, B., Stevens, H., Papastathopoulos, I. and Nolan, M. F. (2020), ‘Grid cells are modulated by local head direction’, *Nature Communications* **11**, 1–14.
- Gerlei, K. Z., Brown, C. M., Sürmeli, G. and Nolan, M. F. (2021), ‘Deep entorhinal cortex: From circuit organization to spatial cognition and memory’, *Trends in Neurosciences* **44**, 876–887.
- Gneiting, T. and Raftery, A. E. (2007), ‘Strictly proper scoring rules, prediction, and estimation’, *Journal of the American statistical Association* **102**, 359–378.
- Gradshteyn, I. S. and Ryzhik, I. M. (2014), *Table of Integrals, Series, and Products*, Academic press.
- Hafting, T., Fyhn, M., Molden, S., Moser, M.-B. and Moser, E. I. (2005), ‘Microstructure of a spatial map in the entorhinal cortex’, *Nature* **436**, 801.
- Kass, R. E. and Ventura, V. (2001), ‘A spike-train probability model’, *Neural computation* **13**, 1713–1720.
- Kropff, E., Carmichael, J. E., Moser, M.-B. and Moser, E. I. (2015), ‘Speed cells in the medial entorhinal cortex’, *Nature* **523**, 419–424.
- Lindgren, F., Bolin, D. and Rue, H. (2022), ‘The SPDE approach for Gaussian and non-Gaussian fields: 10 years and still running’, *Spatial Statistics* **50**, 100599.
- Lindgren, F., Rue, H. and Lindström, J. (2011), ‘An explicit link between Gaussian fields and Gaussian Markov random fields: the stochastic partial differential equation approach (with discussion)’, *J. Roy. Statist. Soc., B* **73**, 423–498.
- Lindgren, G. (2012), *Stationary stochastic processes: theory and applications*, CRC Press.
- Moser, E. I., Moser, M.-B. and McNaughton, B. L. (2017), ‘Spatial representation in the hippocampal formation: A history’, *Nat. Neurosci.* **20**, 1448–1464.
- Rougier, J. (2008), ‘Efficient emulators for multivariate deterministic functions’, *Journal of Computational and Graphical Statistics* **17**, 827–843.

- Rue, H. and Held, L. (2005), *Gaussian Markov Random Fields: Theory and Applications*, Chapman and Hall/CRC.
- Rue, H., Martino, S. and Chopin, N. (2009), ‘Approximate Bayesian inference for latent Gaussian models by using integrated nested Laplace approximations’, *Journal of the royal statistical society: Series b (statistical methodology)* **71**, 319–392.
- Rule, M. E., Vayalambone, P. C., Krstulovic, M., Bauza, M., Krupic, J. and O’Leary, T. (2023), ‘Variational log-gaussian point-process methods for grid cells’, *bioRxiv* pp. 2023–03.
- Sargolini, F., Fyhn, M., Hafting, T., McNaughton, B. L., Witter, M. P., Moser, M.-B. and Moser, E. I. (2006), ‘Conjunctive representation of position, direction, and velocity in entorhinal cortex’, *Science* **312**, 758–762.
- Searle, S. R. (1979), ‘On inverting circulant matrices’, *Linear Algebra and its Applications* **25**, 77–89.
- Siegle, J. H., López, A. C., Patel, Y. A., Abramov, K., Ohayon, S. and Voigts, J. (2017), ‘Open ephys: an open-source, plugin-based platform for multichannel electrophysiology’, *Journal of neural engineering* **14**, 045003.
- Simpson, D., Illian, J. B., Lindgren, F., Sørbye, S. H. and Rue, H. (2016), ‘Going off grid: computationally efficient inference for log-Gaussian Cox processes’, *Biometrika* **103**, 49–70.
- Solstad, T., Boccara, C. N., Kropff, E., Moser, M.-B. and Moser, E. I. (2008), ‘Representation of geometric borders in the entorhinal cortex’, *Science* **322**, 1865–1868.
- Stein, M. L. (1999), *Interpolation of Spatial Data: Some Theory for Kriging*, Springer Series in Statistics, New York.
- Tukker, J. J., Beed, P., Brecht, M., Kempster, R., Moser, E. I. and Schmitz, D. (2022), ‘Microcircuits for spatial coding in the medial entorhinal cortex’, *Physiological Reviews* **102**, 653–688.
- Yuan, Y., Bachl, F. E., Lindgren, F., Borchers, D. L., Illian, J. B., Buckland, S. T., Rue, H. and Gerrodette, T. (2017), ‘Point process models for spatio-temporal distance sampling data from a large-scale survey of blue whales’, *The Annals of Applied Statistics* **11**, 2270–2297.